*buildings*

MDPI

*Article*

# Optimization of Low-Heat Cementitious Materials Based on Construction Spoil Using Response Surface Methodology

**Xiangsai Guo [1], Qiang Zeng [2], Desheng Jin [1], Hao Wu [2,*], Chao Wang [1] and Zhiwei Song [1]**

[1] China Railway 16th Bureau Group Co., Ltd., Beijing 100018, China
[2] School of Civil and Architectural Engineering, East China Jiaotong University, Nanchang 330013, China
* Correspondence: 2023018085901056@ecjtu.edu.cn

**Abstract**

To address the problem of temperature cracking caused by the concentrated release of hydration heat in mass concrete, this study developed a low-heat composite cementitious material (CWCM) by partially replacing conventional mineral admixtures with construction spoil. A multi-factor synergistic optimization design based on response surface methodology (RSM) was conducted. The water–binder ratio, spoil replacement ratio, curing temperature, and ball-milling time were selected as influencing factors, while the 28-day flexural strength, 28-day compressive strength, and 72 h cumulative hydration heat were used as response variables. A four-factor, three-level Box–Behnken model was established. The results show that the regression model exhibits good fitting performance, and the prediction errors between the predicted and experimental values of all response variables are within a reasonable range. Under the optimized mixture proportion (15% spoil replacement), the system achieves a 28-day compressive strength of 61.03 MPa, while the 72 h cumulative hydration heat is reduced by approximately 15%, meeting the requirements for low-heat cement. Microstructural analyses using XRD, SEM, and TG/DTG indicate that a decrease in the Ca/Si ratio and an increase in the Al/Si ratio promote the formation of a denser C-(A)-S-H gel structure, enhancing the pozzolanic reaction. This mechanism plays a key role in achieving the synergistic regulation of strength enhancement and hydration heat reduction. Compared with conventional fly ash or slag systems, this study innovatively utilizes construction spoil as a partial substitute for traditional mineral admixtures. While maintaining satisfactory mechanical performance, the proposed system effectively reduces hydration heat release, providing a new pathway for temperature control design in mass concrete engineering and high-value resource utilization of construction waste.

**Keywords:** construction waste; response surface methodology; low-heat cement; hydration mechanism; mass concrete

Check for updates

Academic Editors: Zhikang Bao, Prince Antwi-Afari and Timothy Olawumi

Received: 11 February 2026
Revised: 10 March 2026
Accepted: 11 March 2026
Published: 22 March 2026
Corrected: 2 April 2026

**Copyright:** © 2026 by the authors. Licensee MDPI, Basel, Switzerland. This article is an open access article distributed under the terms and conditions of the Creative Commons Attribution (CC BY) license.

## 1. Introduction

Mass concrete, owing to its excellent structural integrity and load-bearing capacity, is indispensable in major infrastructure such as hydraulic hubs, foundations of super-high-rise buildings, and offshore bridge piers. However, the substantial heat released during cement hydration readily generates pronounced temperature gradients between the interior and the surface of concrete, leading to thermal stresses that may exceed the material's tensile strength and ultimately cause irreversible thermal cracking. This issue is particularly critical for key facilities, including large hydropower dams and nuclear

containment structures, where cracks can markedly compromise impermeability and durability, thereby threatening long-term service safety [1–4]. Reports indicate that more than 60% of distress in mass-concrete projects is directly associated with inadequate control of hydration heat. Consequently, developing cementitious binders that combine low heat evolution with adequate mechanical performance has become a central strategy to mitigate this engineering challenge.

Conventional low-heat binder systems typically rely on industrial by-products such as fly ash and ground granulated blast-furnace slag as supplementary cementitious materials. However, their availability and quality are strongly influenced by regional industrial layouts, resulting in uneven supply and considerable variability, which hampers reliable application in large-scale construction [5]. In parallel, China's infrastructure development has generated an annual production of construction spoil exceeding 3.5 billion tons, with cumulative stockpiles surpassing 10 billion tons. Current disposal practices remain dominated by open-air dumping and landfilling, which not only consume substantial land resources but also induce environmental and geohazard risks, including dust pollution and landslides (Figure 1) [6,7]. Therefore, high-value valorization of construction spoil has become an important research priority for advancing green construction and alleviating ecological burdens.

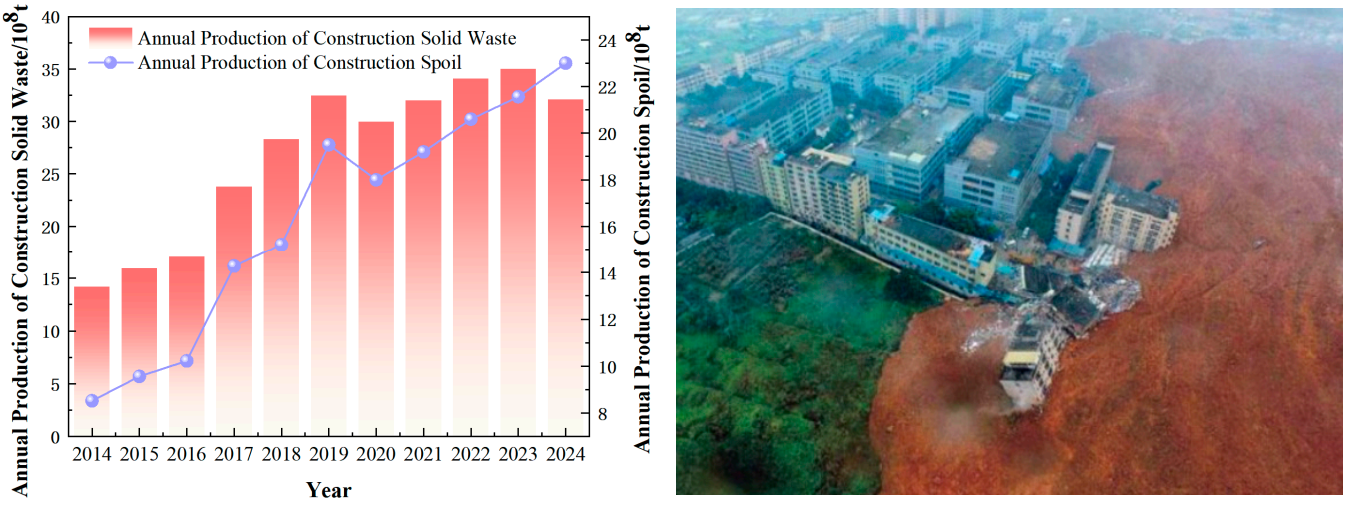



**Figure 1.** Annual generation of construction spoil in China from 2014 to 2024 and spoil-stockpiling-induced landslides.

Construction spoil is rich in clay minerals such as kaolinite and montmorillonite. With appropriate pretreatment, the reactive $SiO_2$ and $Al_2O_3$ fractions can be activated, conferring potential value as supplementary constituents in cement-based materials while contributing to a reduction in the heat released during cement hydration [8]. In recent years, both domestic and international studies have explored the partial replacement of cement with construction spoil. Regarding activation strategies, Wang Hailiang et al. [9] investigated the effectiveness of calcination–grinding pretreatments for stimulating reactive components in engineering spoil and evaluated reactivity using alkaline dissolution and the pozzolanic activity index. They reported that calcination induces structural depolymerization of clay minerals (e.g., kaolinite), increases the content of amorphous $SiO_2$ and $Al_2O_3$, and markedly improves the activity index; nevertheless, the overall reactivity remains lower than that of conventional highly active mineral admixtures, classifying the material as a medium- to low-reactivity aluminosilicate. Pan Dong [10] examined particle-size evolution during fine grinding and its influence on cement hydration. The results showed that increasing the specific surface area enhances the dissolution of reactive Si and Al and

accelerates early pozzolanic reactions, indicating an activation effect; however, further intensification of grinding yields diminishing gains, suggesting that mechanical activation alone is insufficient to achieve efficient high-level activation.

In terms of mechanical performance, Guo et al. [11] and Jiang [12] systematically evaluated the effects of partially replacing cement with construction spoil using unconfined compressive strength and flexural strength tests. Their results indicate that at spoil dosages not exceeding 15–20%, the 28-day compressive strength can reach 20–30 MPa, which generally meets the requirements for ordinary structural concrete; however, higher replacement levels constrain strength development and still lag behind the reference cement concrete. Yang Tao et al. [13] further combined macroscopic mechanical testing with microstructural characterization to elucidate strength formation mechanisms in stabilized spoil-based materials. They found that when the spoil content is maintained at 10–20%, the filler effect can improve particle packing, reduce porosity by approximately 10–20%, and increase the 28-day compressive strength by 5–15% relative to systems without filler; by contrast, when the spoil content exceeds 30%, the 28-day compressive strength decreases by 15–30%, indicating pronounced mechanical deterioration.

With respect to durability, Wang Hailiang et al. [14] assessed the applicability of construction spoil as a cementitious addition through freeze–thaw resistance and water impermeability tests. They reported that when the spoil content is controlled below 20%, both freeze–thaw resistance and impermeability can be improved, primarily due to pore-structure refinement induced by fine-particle filling; when the content exceeds 20%, the internal structure becomes looser and durability indices decline appreciably, thereby restricting engineering applicability. Regarding hydration-heat mitigation, studies by Cao Ke, Wang Jinxin, and co-workers [15,16] using isothermal calorimetry and hydration-heat measurements indicate that reactive $SiO_2$ and $Al_2O_3$ in construction spoil can participate in later-stage pozzolanic reactions, reducing the early heat-release rate and peak heat output. This behavior effectively suppresses heat accumulation and suggests promising potential for low-heat regulation, particularly for mass concrete or other applications with stringent low-heat requirements. Chen Deng et al. [17] further demonstrated, via calorimetry and microstructural analyses, that calcined spoil can partially substitute conventional mineral admixtures in blended binder systems, decreasing the main exothermic peak by approximately 15–30%, delaying the peak occurrence by about 6–12 h, and reducing the 72 h cumulative hydration heat by 10–20% [18].

In recent years, extensive research has been conducted worldwide on low-heat cementitious materials and the resource utilization of solid wastes. Materials such as fly ash, slag, and calcined clay have been widely applied in low-heat binder systems to reduce hydration heat peaks and improve durability. Meanwhile, several studies have attempted to partially replace cement with construction waste or spoil in order to achieve solid waste recycling. However, existing studies still exhibit several limitations.

First, most previous studies employed single-factor experimental approaches to investigate the influence of replacement ratios on strength or durability. Multi-factor coupled optimization designs are rarely adopted, making it difficult to establish systematic correlations between material performance and hydration heat evolution. Second, existing literature mainly focuses on mechanical or durability performance evaluation, while the influence of construction spoil participation in hydration reactions on hydration heat release kinetics remains insufficiently explored, particularly from the perspective of microstructural evolution. In addition, quantitative design methods that can simultaneously ensure strength development and low hydration heat release for mass concrete applications are still limited.

Therefore, there remains a lack of a systematic design strategy capable of achieving high-volume utilization of construction spoil while simultaneously optimizing mechanical performance and hydration heat regulation behavior. This research gap has limited the practical application of construction spoil in mass concrete engineering.

To address these issues, this study aims to develop a novel low-heat construction-spoil-based composite cementitious material. A multi-factor coupled response surface optimization model was established to systematically investigate the effects of water–binder ratio (0.275–0.325), spoil replacement ratio (0–30%), curing temperature (20–80 °C), and ball-milling time (0–10 min) on the 28-day flexural strength, compressive strength, and 72 h hydration heat. The relationship between strength development and hydration heat regulation was established. In addition, microstructural characterization techniques, including XRD, SEM, and TG/DTG, were employed to reveal the internal mechanisms of spoil activation and pore structure evolution during hydration. Compared with traditional fly ash or slag systems, the material system developed in this study exhibits advantages such as abundant raw material sources, strong regional adaptability, large-scale waste utilization capacity, and significant potential for carbon reduction, providing a new theoretical basis and technical pathway for the high-value utilization of construction spoil.

## 2. Experimental Program

### *2.1. Materials and Experimental Equipment*

Construction spoil: The construction spoil used in this study was collected from Xuchang, Henan Province, China. The spoil was first dried in an oven at 105 °C for 24 h, followed by crushing using a mechanical crusher and sieving through a 3 mm sieve. The processed material was then subjected to mechanical grinding using a planetary ball mill with a rotation speed of 500 r/min and a milling time of 5 min. The particle size distribution of the ground construction spoil was measured using a Bettersize 3000Plus particle size analyzer (Bettersize Instruments Ltd., Dandong, China). The particle size distribution results are shown in Figure 2.

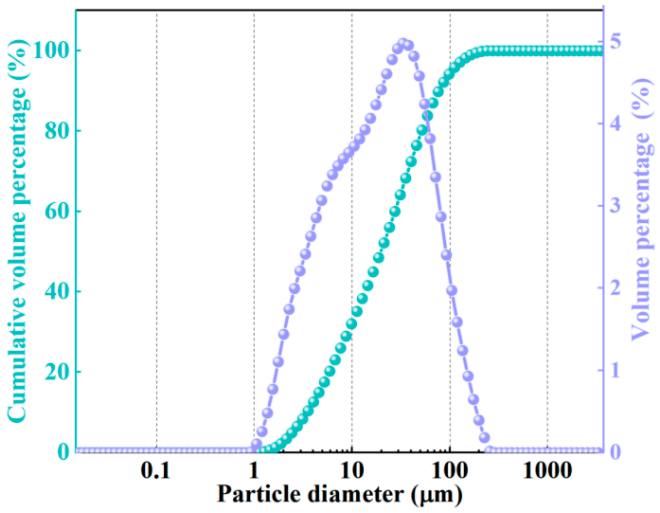



**Figure 2.** Particle-size distribution of the construction spoil.

Ordinary Portland cement (P.O 42.5): The cement used in this study was supplied by Anhui China Conch Cement Co., Ltd., Anhui China, with a specific surface area of 330 $m^2$/kg.

The chemical compositions of the construction spoil and cement were determined by X-ray fluorescence spectroscopy (XRF), and the results are presented in Table 1.

**Table 1.** Chemical composition of the construction spoil and cement (wt.%).

| Oxide Composition | $SiO_2$ | $Al_2O_3$ | $Fe_2O_3$ | CaO | MgO | $SO_3$ | $K_2O$ | LOI | Others |
|---|---|---|---|---|---|---|---|---|---|
| construction spoil | 67.44 | 18.80 | 6.09 | 1.22 | 1.83 | 0.05 | 2.85 | - | 1.72 |
| cement | 22.06 | 6.14 | 3.43 | 62.98 | 2.77 | 2.12 | - | 0.5 | - |

Standard sand: ISO standard sand for cement testing was used in accordance with the relevant testing specifications.

The mineralogical composition of the construction spoil was analyzed using X-ray diffraction (XRD). The scanning range was 5–90° (2θ), and the results are shown in Figure 3. The analysis indicates that the main mineral phases present in the construction spoil include quartz (Quartz), muscovite (Muscovite), albite (Albite), kaolinite (Kaolinite), and calcite (Calcite).

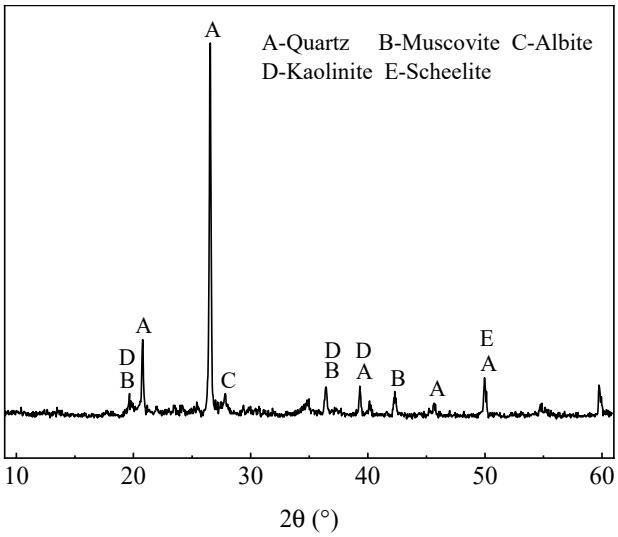



**Figure 3.** XRD Analysis of Construction waste.

*2.2. Experimental Design*

The factor ranges selected in this study were determined based on preliminary experiments and reported literature, covering the transition range from low to high material reactivity to ensure sufficient optimization space and statistical validity of the response surface model.

To ensure the relevance of the selected variables, several potential influencing factors were evaluated based on preliminary experiments. Ball-milling time and curing temperature were identified as the key variables for the following reasons.

First, construction spoil is a medium-to-low reactivity aluminosilicate material whose reactivity is strongly affected by mechanical activation. Ball-milling time directly determines the particle-specific surface area and the exposure of potential reactive components, thereby influencing the pozzolanic reaction rate and the amount of gel formation.

Second, curing temperature significantly affects the kinetics of cement hydration. In mass concrete engineering, elevated temperatures may accelerate the occurrence of hydration heat peaks and influence long-term structural stability; therefore, this parameter has important engineering implications [19].

In contrast, the fineness modulus is intrinsically related to ball-milling time, and its influence has been indirectly reflected through the ball-milling variable [20]. Moreover, slag content is not a core component of the studied system, as this research primarily focuses on the resource utilization of construction spoil. Therefore, ball-milling time and curing

temperature were selected as independent variables based on both material mechanism considerations and engineering application relevance.

To ensure scientific validity and engineering relevance in the experimental design, the selection of factor levels was based on previous studies and engineering application considerations [21,22]. The water–binder ratio range (0.275–0.325) was selected according to the commonly used range for high-performance cementitious materials [23], ensuring adequate strength development while avoiding insufficient workability caused by excessively low water–binder ratios. The construction spoil replacement ratio was set to 0–30%, based on previous studies indicating that mechanical performance significantly decreases when the replacement ratio exceeds approximately 30% [11–14]. The curing temperature range (20–80 °C) was designed to simulate the internal temperature rise conditions in mass concrete structures, where 80 °C represents an extreme temperature condition [24]. The ball-milling time was selected as 0–10 min based on previous studies on the mechanical activation of aluminosilicate materials [9,10], which can effectively increase the specific surface area while avoiding excessive energy consumption caused by over-grinding [25].

To further improve the workability of CWCM, the present study, building on our preliminary findings, employed Design-Expert software 13 to perform response surface analysis based on the Box–Behnken design, with the aim of obtaining CWCM with satisfactory mechanical performance. The 28-day flexural strength (Y1), 28-day compressive strength (Y2), and 72 h cumulative hydration heat (Y3) were selected as the response variables, while the water-to-binder ratio (A), construction spoil replacement (B), curing temperature (C), and ball-milling time (D) were taken as the independent factors. A four-factor, three-level response surface optimization program was established, and the factor levels are listed in Table 2.

**Table 2.** Factors and levels used in the experimental design.

| Factor | Level | | |
|---|---|---|---|
| | **−1** | **0** | **1** |
| Water-to-binder ratio (A) | 0.275 | 0.3 | 0.325 |
| Construction spoil replacement (B, %) | 0 | 15 | 30 |
| Curing temperature (C, °C) | 20 | 50 | 80 |
| Ball-milling time (D, min) | 0 | 5 | 10 |

### *2.3. Specimen Preparation and Testing*

#### 2.3.1. Specimen Preparation

Prior to mixing, the construction spoil was pretreated by oven-drying at 105 °C, followed by ball milling at 500 r/min for 5 min to obtain a fine powder. The processed spoil and the pre-weighed cement were then placed in a mortar mixer and dry-mixed for 60 s until homogeneous. Subsequently, the required amount of water was added, and the mixture was stirred at low speed for 60 s. After scraping the paste adhering to the bowl and the material deposited at the bottom, the mixture was further mixed at low speed for 90 s while ISO standard sand was gradually introduced. The adhered mortar and bottom deposits were scraped again, after which the mortar was mixed at low speed for 30 s and then at high speed to ensure uniformity. The fresh mortar was cast into 40 mm × 40 mm × 160 mm molds, covered with plastic film, and cured at room temperature for 24 h before demolding. Finally, the specimens were transferred to a standard curing chamber and cured to the designated ages for subsequent mechanical testing and microstructural characterization. The overall experimental workflow is illustrated in Figure 4.

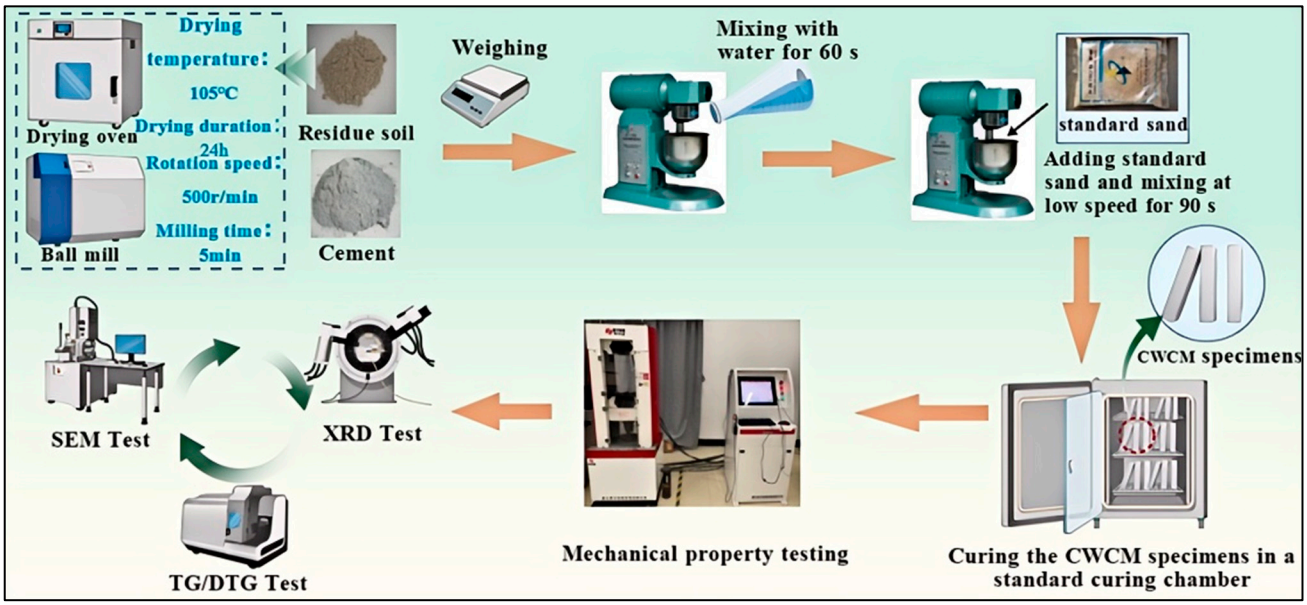



**Figure 4.** Schematic diagram of the experimental workflow.

2.3.2. Mechanical Tests

The mechanical performance of CWCM was evaluated in terms of flexural and compressive strengths. Prismatic specimens with dimensions of 40 mm × 40 mm × 160 mm were cured in a standard curing chamber to the designated ages and then tested for flexural strength in accordance with GB/T 17671-2021 (ISO method for strength testing of cement mortar). After the flexural test, each prism was fractured into two halves, and one half was subsequently used for the compressive strength test. Throughout the testing procedure, curing temperature and loading rate were strictly controlled to ensure data accuracy and repeatability.

2.3.3. Heat of Hydration

The isothermal calorimetry method was employed to measure the hydration heat using a TAM-Air calorimeter. Cement paste samples of CWCM were prepared with a water–binder ratio of 0.40, and the fresh paste was immediately placed in the calorimeter at a constant temperature of 20 °C. The calorimeter continuously monitored and recorded the heat flow rate, while the cumulative hydration heat was simultaneously calculated.

It should be noted that the hydration heat test adopted a water–binder ratio of 0.40, mainly due to the requirement of adequate fluidity and homogeneous mixing during isothermal calorimetry testing. Lower water–binder ratios may lead to insufficient dispersion of the paste during testing, which could affect the stability and reproducibility of the heat evolution curve. In this study, the w/b = 0.40 condition was used only for comparative analysis of hydration heat behavior among different mixtures and was not involved in the response surface optimization model. The water–binder ratio range used in the optimization model (0.275–0.325) was designed for comprehensive performance evaluation, meaning that the two water–binder ratio conditions served different research objectives.

2.3.4. X-Ray Diffraction (XRD)

Phase assemblages were analyzed using a D/MAX-IIIA X-ray diffractometer (Almelo, The Netherlands, Malvern Panalytical B.V.)with Cu Kα radiation (λ = 1.54 A). The instrument was operated at 20 kV and 40 mA. Data were collected over a 2θ range of 5–90° at a scanning rate of 4°/min with a step size of 0.04°.

2.3.5. Scanning Electron Microscopy (SEM)

Microstructural features and hydration products were examined using a HITACHI SU8010 scanning electron microscope. Prior to observation, the specimens were polished and gold-sputtered. SEM imaging was performed at an accelerating voltage of 20 kV.

2.3.6. Thermogravimetry/Differential Thermogravimetry (TG/DTG)

Hydration products were semi-quantitatively assessed by TG/DTG using a Mettler Toledo thermal analyzer (Switzerland). The mortar specimens were ground into powder and sieved through a 45 μm mesh. The prepared samples were heated from ambient temperature to 1000 °C at a rate of 10 °C/min under a nitrogen atmosphere, and the TG and DTG curves were used to interpret the to interpret the results.

To systematically reveal the hydration mechanism and performance evolution of construction-spoil-based cementitious materials, a multi-scale characterization framework was established. XRD was first employed to identify the types and variations in crystalline hydration products in order to evaluate pozzolanic reaction intensity and phase transformation characteristics. SEM was used to observe the morphology of hydration products, while EDS elemental analysis was conducted to calculate Ca/Si and Al/Si atomic ratios, thereby revealing variations in gel compactness and structural stability. TG/DTG analysis was applied to evaluate mass losses in different temperature ranges and to semi-quantitatively estimate bound water content and $Ca(OH)_2$ consumption, providing thermodynamic evidence for the pozzolanic reaction process. In addition, isothermal calorimetry was used to analyze hydration heat release rates and cumulative heat evolution to assess the low-heat regulation performance of the system. These methods complement each other at the levels of phase composition, morphology, thermal stability, and kinetics, providing comprehensive support for the proposed strength–low heat synergistic regulation mechanism.

## 3. Results and Discussion

### *3.1. Response Surface Results*

The mixture proportions designed using the Box–Behnken response surface methodology and the corresponding response values are summarized in Table 3. The experimental matrix comprised 24 factorial runs (Runs 1–24) and five center-point replicates (Runs 25–29). Quadratic polynomial regression models were established for the selected responses as functions of the four factors, and the fitted equations are given in Equations (1)–(4).

$$Y = \beta_0 + \sum_{i=1}^{k} \beta_i X_i + \sum_{i=1}^{k} \beta_{ii} {X_i}^2 + \sum_{i<j}^{k} \beta_{ij} X_i X_j \quad (1)$$

**Table 3.** Mixture proportions and results of the Box–Behnken design.

| Run | Factors | | | | Experimental Values | | | Predicted Values | | |
|---|---|---|---|---|---|---|---|---|---|---|
| | A | B | C | D | Y1 | Y2 | Y3 | Y1 | Y2 | Y3 |
| 1 | −1 | −1 | 0 | 0 | 10.60 | 59.37 | 245.0 | 10.75 | 59.58 | 240.3 |
| 2 | 1 | −1 | 0 | 0 | 9.32 | 56.27 | 230.0 | 9.40 | 56.46 | 228.4 |
| 3 | −1 | 1 | 0 | 0 | 10.46 | 60.87 | 205.0 | 10.42 | 60.10 | 207.1 |
| 4 | 1 | 1 | 0 | 0 | 9.01 | 50.61 | 195.0 | 8.90 | 49.84 | 193.6 |
| 5 | 0 | 0 | −1 | −1 | 10.88 | 56.44 | 180.0 | 10.97 | 56.69 | 180.2 |
| 6 | 0 | 0 | 1 | −1 | 8.43 | 58.86 | 290.0 | 10.42 | 58.71 | 289.8 |
| 7 | 0 | 0 | −1 | 1 | 10.76 | 60.87 | 190.0 | 10.82 | 60.45 | 189.5 |
| 8 | 0 | 0 | 1 | 1 | 8.56 | 53.00 | 310.0 | 10.51 | 52.18 | 309.3 |
| 9 | −1 | 0 | 0 | −1 | 11.09 | 61.06 | 220.0 | 11.16 | 61.04 | 220.1 |

**Table 3.** *Cont.*

| Run | Factors | | | | Experimental Values | | | Predicted Values | | |
|---|---|---|---|---|---|---|---|---|---|---|
| | A | B | C | D | Y1 | Y2 | Y3 | Y1 | Y2 | Y3 |
| 10 | 1 | 0 | 0 | −1 | 10.59 | 54.82 | 200.0 | 9.62 | 54.62 | 200.3 |
| 11 | −1 | 0 | 0 | 1 | 10.97 | 59.35 | 240.0 | 11.03 | 59.93 | 239.9 |
| 12 | 1 | 0 | 0 | 1 | 9.69 | 52.58 | 215.0 | 9.71 | 52.97 | 215.2 |
| 13 | 0 | −1 | −1 | 0 | 10.51 | 58.74 | 210.0 | 10.52 | 58.31 | 209.8 |
| 14 | 0 | 1 | −1 | 0 | 10.11 | 56.03 | 170.0 | 10.25 | 57.53 | 170.4 |
| 15 | 0 | −1 | 1 | 0 | 8.29 | 58.59 | 330.0 | 10.23 | 57.46 | 329.7 |
| 16 | 0 | 1 | 1 | 0 | 7.60 | 51.34 | 260.0 | 9.67 | 52.14 | 260.1 |
| 17 | −1 | 0 | −1 | 0 | 11.45 | 62.42 | 195.0 | 11.46 | 61.88 | 195.2 |
| 18 | 1 | 0 | −1 | 0 | 9.93 | 55.24 | 175.0 | 9.83 | 54.88 | 175.3 |
| 19 | −1 | 0 | 1 | 0 | 9.87 | 57.90 | 280.0 | 10.84 | 58.45 | 279.9 |
| 20 | 1 | 0 | 1 | 0 | 8.53 | 51.32 | 250.0 | 9.60 | 52.06 | 250.2 |
| 21 | 0 | −1 | 0 | −1 | 10.41 | 61.74 | 240.0 | 10.29 | 62.28 | 240.0 |
| 22 | 0 | 1 | 0 | −1 | 10.03 | 52.88 | 190.0 | 9.97 | 52.47 | 190.1 |
| 23 | 0 | −1 | 0 | 1 | 10.43 | 53.52 | 270.0 | 10.36 | 54.13 | 269.9 |
| 24 | 0 | 1 | 0 | 1 | 9.8623 | 58.19 | 225.0 | 9.85 | 57.84 | 225.0 |
| 25 | 0 | 0 | 0 | 0 | 10.14 | 60.22 | 235.0 | 9.95 | 61.00 | 235.0 |
| 26 | 0 | 0 | 0 | 0 | 10.03 | 60.49 | 234.0 | 9.95 | 61.00 | 235.4 |
| 27 | 0 | 0 | 0 | 0 | 9.22 | 61.04 | 236.0 | 9.95 | 61.00 | 234.1 |
| 28 | 0 | 0 | 0 | 0 | 10.22 | 61.66 | 235.0 | 9.95 | 61.00 | 235.2 |
| 29 | 0 | 0 | 0 | 0 | 10.14 | 61.59 | 235.0 | 9.95 | 61.00 | 235.0 |

$Y_1$ represents the 28-day flexural strength (MPa):

$$\begin{aligned} Y_1 &= 9.95 - 0.62A - 0.21B - 1.03C - 0.10D - 0.04AB \\ &+0.04AC - 0.20AD - 0.07BC - 0.05BD + 0.06CD \\ &+0.3241A^2 - 0.28799B^2 - 0.5023C^2 + 0.3482D^2 \end{aligned} \quad (2)$$

$Y_2$ represents the 28-day compressive strength (MPa):

$$\begin{aligned} Y_2 &= 61 - 3.35A - 1.53B - 1.56C - 0.69D - 1.79AB \\ &+0.15AC - 0.13AD - 1.13BC + 3.38BD - 2.57CD \\ &-2.02A^2 - 2.48B^2 + 2.16C^2 - 1.84D^2 \end{aligned} \quad (3)$$

$Y_3$ represents the 72 h cumulative hydration heat (J/g):

$$\begin{aligned} Y_3 &= 235.0 - 12.5A - 8.2B + 27.3C + 4.7D - 6.8A^2 \\ &-5.1B^2 + 9.6C^2 - 2.3D^2 - 3.5AB - 15.2AC + 2.1AD \\ &+7.8BC - 1.9BD - 4.3CD + 0.32A^2 - 0.29B^2 - 0.50C^2 \\ &+0.35D^2 \end{aligned} \quad (4)$$

where:

$Y_1$ is the 28-day flexural strength, MPa;
$Y_2$ is the 28-day compressive strength, MPa;
$Y_3$ is the 72 h cumulative hydration heat, J/g;
$A$ is the water-to-binder ratio;
$B$ is the construction spoil content, %;
$C$ is the curing temperature, °C;
$D$ is the ball-milling time, min.

### 3.2. Analysis of Variance

Tables 4 and 5 summarize the ANOVA results for the quadratic polynomial regression models. As shown in Tables 4 and 5, the model F-values were F(Y1) = 11.54 with $p$(Y1) < 0.0001, F(Y2) = 33.21 with $p$(Y2) < 0.0001, and F(Y3) = 33.21 with $p$(Y3) < 0.0001, indicating that all models are highly significant ($p$ < 0.0001). The lack-of-fit term in Tables 4 and 5 reflects the probability that the experimental data deviate from the proposed model. In this study, the lack-of-fit statistics were F(Y1) = 0.7481 with $p$(Y1) = 0.6779, F(Y2) = 2.25 with $p$(Y2) = 0.2253, and F(Y3) = 1.83 with $p$(Y3) = 0.2864, suggesting that the lack of fit is not significant ($p$ > 0.05). Therefore, the fitted models adequately describe the experimental data, and the experimental design is considered appropriate. For the 28-day flexural strength response (Y1), factors A, B, and C were significant, with A and C being highly significant, indicating that these two factors exert pronounced effects on the 28-day flexural strength of CWCM mortar. For the 28-day compressive strength response (Y2), factors A, B, C, and D were significant, among which A, B, and C were highly significant, demonstrating that these three factors strongly influence the 28-day compressive strength. For the hydration heat response (Y3), factors A, C, and D were significant, with A and C being highly significant, implying that the water-to-binder ratio and curing temperature have dominant effects on hydration heat, while the ball-milling time has a statistically significant effect.

**Table 4.** ANOVA for the response surface models.

| Source of Variation | Sum of Squares | | | Degrees of Freedom | | | Mean Square | | |
|---|---|---|---|---|---|---|---|---|---|
| | Y1 | Y2 | Y3 | Y1 | Y2 | Y3 | Y1 | Y2 | Y3 |
| model | 22.6 | 364.0 | 9850.2 | 14.0 | 14.0 | 14.0 | 1.6 | 26.0 | 703.6 |
| A | 4.5 | 134.3 | 2850.4 | 1.0 | 1.0 | 1.0 | 4.5 | 134.3 | 2850.4 |
| B | 0.5 | 27.9 | 650.2 | 1.0 | 1.0 | 1.0 | 0.5 | 27.9 | 650.2 |
| C | 12.7 | 29.3 | 3520.8 | 1.0 | 1.0 | 1.0 | 12.7 | 29.3 | 3520.8 |
| D | 0.1 | 5.8 | 320.6 | 1.0 | 1.0 | 1.0 | 0.1 | 5.8 | 320.6 |
| AB | 0 | 12.8 | 45.3 | 1.0 | 1.0 | 1.0 | 0 | 12.8 | 45.3 |
| AC | 0 | 0.1 | 125.7 | 1.0 | 1.0 | 1.0 | 0 | 0.1 | 125.7 |
| AD | 0.2 | 0.1 | 28.9 | 1.0 | 1.0 | 1.0 | 0.2 | 0.1 | 28.9 |
| BC | 0 | 5.2 | 85.6 | 1.0 | 1.0 | 1.0 | 0 | 5.2 | 85.6 |
| BD | 0 | 45.7 | 32.4 | 1.0 | 1.0 | 1.0 | 0 | 45.7 | 32.4 |
| CD | 0 | 26.5 | 68.2 | 1.0 | 1.0 | 1.0 | 0 | 26.5 | 68.2 |
| A2 | 0 | 26.5 | 210.5 | 1.0 | 1.0 | 1.0 | 0.7 | 26.5 | 210.5 |
| B2 | 0 | 39.9 | 185.3 | 1.0 | 1.0 | 1.0 | 0.5 | 39.9 | 185.3 |
| C2 | 1.6 | 30.1 | 320.8 | 1.0 | 1.0 | 1.0 | 1.6 | 30.1 | 320.8 |
| D2 | 0.8 | 21.9 | 95.6 | 1.0 | 1.0 | 1.0 | 0.8 | 21.9 | 95.6 |
| Residual | 2.0 | 11.0 | 360.8 | 14.0 | 14.0 | 17.0 | 0.1 | 0.8 | 21.2 |
| Lack of fit | 1.3 | 9.3 | 280.3 | 10.0 | 10.0 | 12.0 | 0.1 | 0.9 | 23.4 |
| Pure error | 0.7 | 1.7 | 80.5 | 4.0 | 4.0 | 5.0 | 0.2 | 0.4 | 16.1 |
| Total | 24.6 | 375.0 | 10,211.0 | 28.0 | 28.0 | 31.0 | - | - | - |

**Table 5.** ANOVA for the response surface model.

| Source of Variation | F | | | *p* | | |
|---|---|---|---|---|---|---|
| | Y1 | Y2 | Y3 | Y1 | Y2 | Y3 |
| model | 11.5 | 33.2 | 33.2 | <0.0001 | <0.0001 | <0.0001 |
| A | 32.5 | 171.6 | 342.1 | <0.0001 | <0.0001 | <0.0001 |
| B | 3.7 | 35.7 | 78.1 | 0.1 | <0.0001 | <0.0001 |

**Table 5.** *Cont.*

| Source of Variation | F | | | *p* | | |
|---|---|---|---|---|---|---|
| | Y1 | Y2 | Y3 | Y1 | Y2 | Y3 |
| C | 91.1 | 37.4 | 422.8 | <0.0001 | <0.0001 | <0.0001 |
| D | 0.8 | 7.3 | 38.5 | 0.4 | 0 | <0.0001 |
| AB | 0 | 16.3 | 5.4 | 0.8 | <0.0001 | 0 |
| AC | 0.1 | 0.1 | 15.1 | 0.8 | 0.7 | 0 |
| AD | 1.1 | 0.1 | 3.5 | 0.3 | 0.8 | 0.1 |
| BC | 0.1 | 6.6 | 10.3 | 0.1 | 0 | 0 |
| BD | 0.1 | 58.4 | 3.9 | 0.8 | 0 | 0.1 |
| CD | 0.1 | 33.8 | 8.2 | 0.3 | <0.0001 | 0 |
| A2 | 4.9 | 33.9 | 25.3 | 0.0 | <0.0001 | 0 |
| B2 | 3.8 | 51.0 | 22.3 | 0.1 | <0.0001 | 0 |
| C2 | 11.7 | 38.5 | 38.5 | 0 | <0.0001 | <0.0001 |
| D2 | 5.6 | 27.9 | 11.5 | 0 | 0 | 0 |
| Residual | - | - | - | - | - | - |
| Lack of fit | 0.7 | 2.3 | 1.8 | 0.7 | 0.2 | 0.3 |
| Pure error | - | - | - | - | - | - |
| Total | - | - | - | - | - | - |

Note: $p < 0.05$ indicates that the investigated factor has a significant effect on the 28-day flexural/compressive strength of CWCM; $p < 0.01$ indicates an extremely significant effect on the 28-day flexural/compressive strength of CWCM; $p < 0.001$ indicates a highly significant effect on hydration heat; and $p < 0.0001$ indicates an extremely significant effect on hydration heat.

### *3.3. Fitting Accuracy Analysis*

Table 6 summarizes the fitting-accuracy metrics of the developed models, showing that all three response surface models exhibit good goodness of fit. The coefficients of determination ($R^2$) for the flexural strength, compressive strength, and hydration heat models were 0.9203, 0.9708, and 0.9642, respectively, and the differences between the adjusted $R^2$ ($R^2$_adj) and predicted $R^2$ ($R^2$_pred) were all below 0.2. The coefficients of variation (C.V., %) were all less than 10%, with the hydration-heat model showing the lowest value (2.15%). In addition, the adequate precision values (signal-to-noise ratio) were greater than 4 for all models, with the hydration-heat model achieving the highest value (28.60). Collectively, these results indicate that the established models provide high predictive accuracy and reliability, and the hydration-heat model in particular exhibits superior stability and robustness against disturbance.

**Table 6.** Fitting-accuracy analysis of the response surface models.

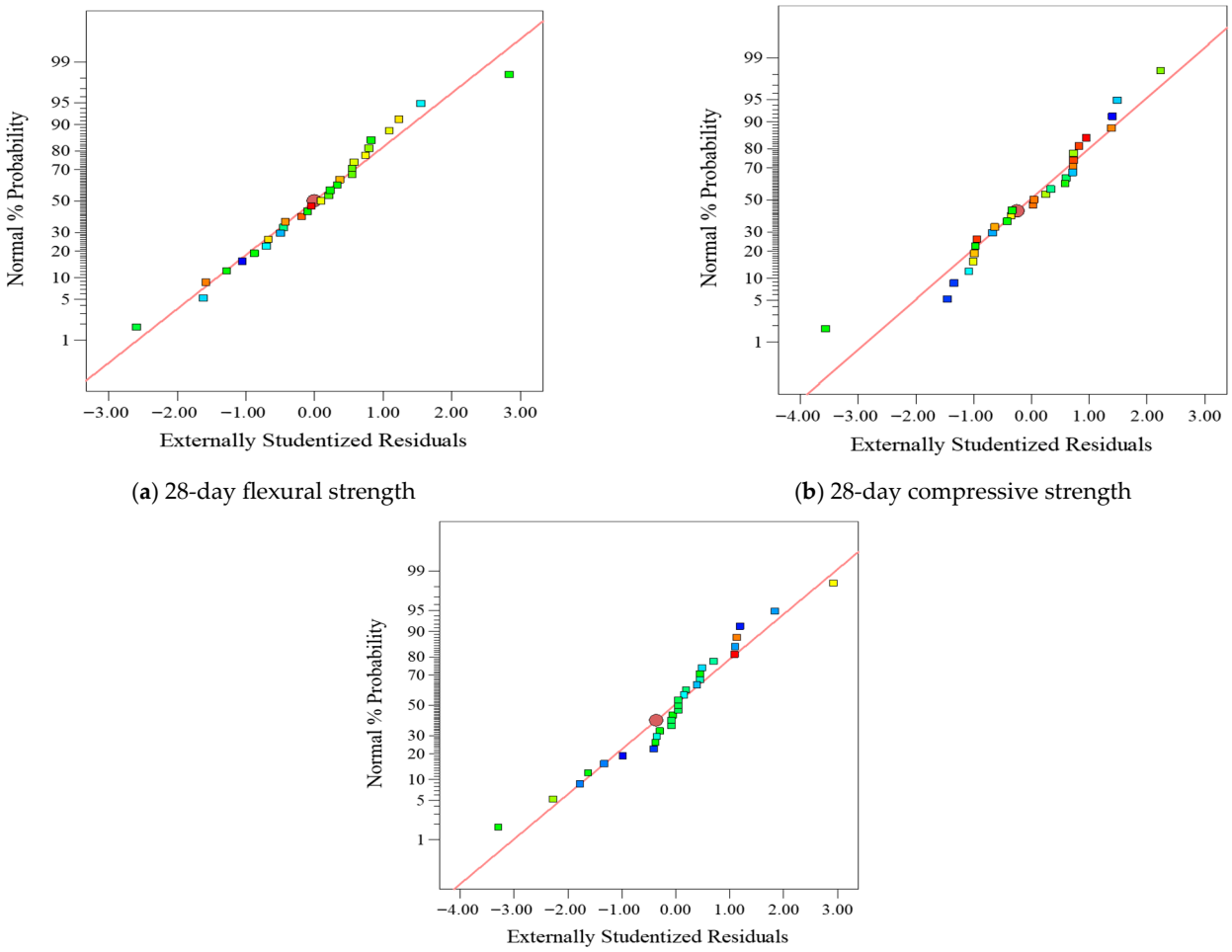
| Response | $R^2$ | $R^2$adj | $R^2$pred | C.V./% | Adequate Precision |
|---|---|---|---|---|---|
| 28-day flexural strength | 0.9203 | 0.8405 | 0.6573 | 3.78 | 13.4245 |
| 28-day compressive strength | 0.9708 | 0.9415 | 0.8501 | 1.54 | 19.5546 |
| 72 h cumulative hydration heat | 0.9642 | 0.9284 | 0.8617 | 2.15 | 28.6012 |

### *3.4. Residual Analysis*

#### 3.4.1. Normal Residual Plot Analysis

Figure 5 presents the residual diagnostics for the response surface regression models developed for the 28-day flexural strength, 28-day compressive strength, and hydration heat of construction-spoil-based mortar specimens. Residual analysis is commonly used to examine model adequacy and the reliability of experimental data; in the absence of outliers, the residuals are expected to follow an approximately normal distribution. As shown in Figure 4, the standardized residuals for all three models fall within the range of

±3, indicating that the data points are randomly scattered without discernible patterns, which supports the rationality of the experimental runs selected by the model. Moreover, the points in the normal probability plots are distributed closely along a straight line, with only a few minor deviations, suggesting that the residuals are approximately normally distributed. These observations confirm that the regression relationships for flexural strength, compressive strength, and hydration heat are adequately captured by the fitted polynomial (or linear) models.




(**a**) 28-day flexural strength

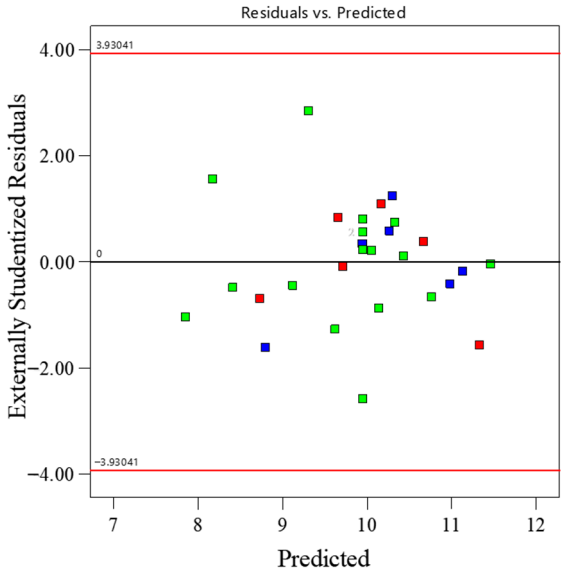
(**b**) 28-day compressive strength

(**c**) 72 h cumulative hydration heat

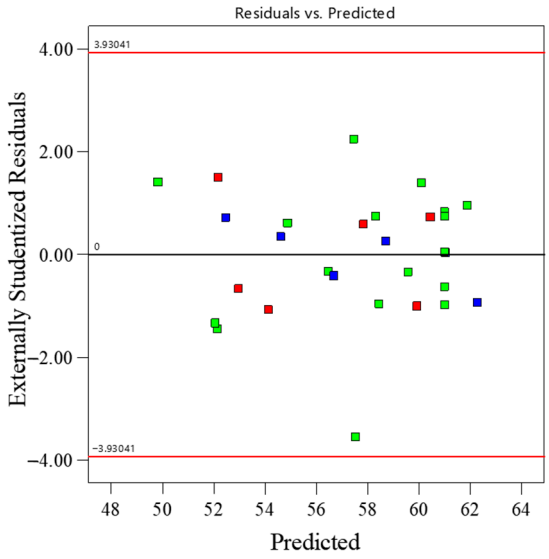
**Figure 5.** Residual analysis of the 28-day flexural/compressive strength and 72 h cumulative hydration heat for construction-spoil-based mortar specimens. (Blue, green, and red squares represent the residual distributions of the models for 28-day flexural strength ($Y_1$), 28-day compressive strength ($Y_2$), and 72 h cumulative hydration heat ($Y_3$), respectively).

### 3.4.2. Residual vs. Predicted Value Analysis

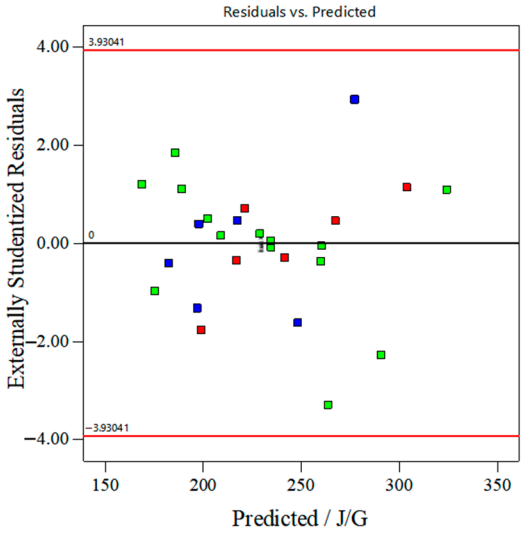
Figure 6 shows the relationship between the residuals and predicted values. The residuals are randomly distributed around the zero line without any apparent funnel-shaped pattern or systematic dispersion trend, indicating that the homoscedasticity assumption of the regression model is satisfied. All externally studentized residuals fall within the range of ±3, and no outliers are detected, demonstrating that the model fitting is stable and reliable.




(**a**) 28-day flexural strength




(**b**) 28-day compressive strength

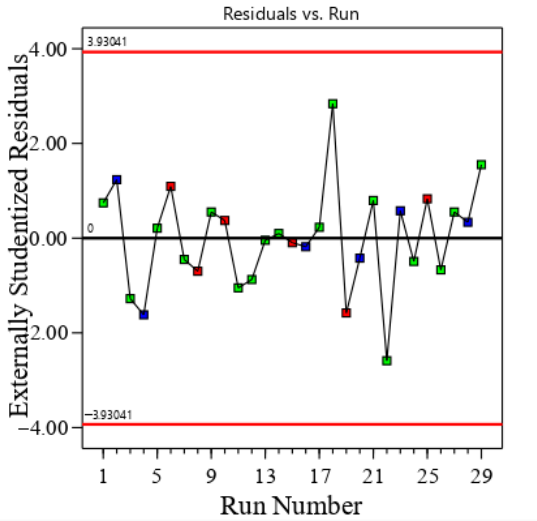



(**c**) 72 h cumulative hydration heat

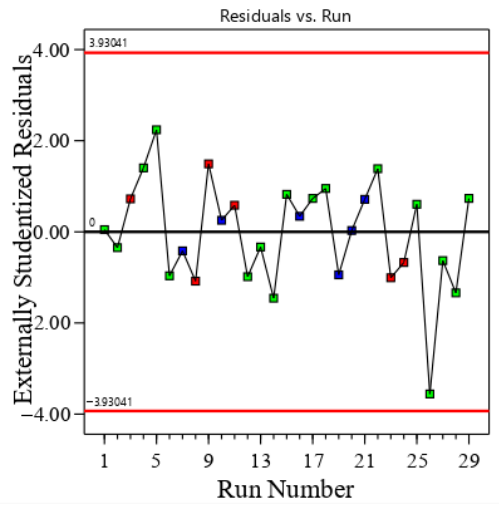
**Figure 6.** Residual vs. predicted value plots for the 28-day flexural strength, 28-day compressive strength, and 72 h cumulative hydration heat of CWCM mortar specimens. (Blue, green, and red of the models for 28-day flexural strength ($Y_1$), 28-day compressive strength ($Y_2$), and 72 h cumulative hydration heat ($Y_3$), respectively).

### 3.4.3. Residual vs. Experimental Run Order Analysis

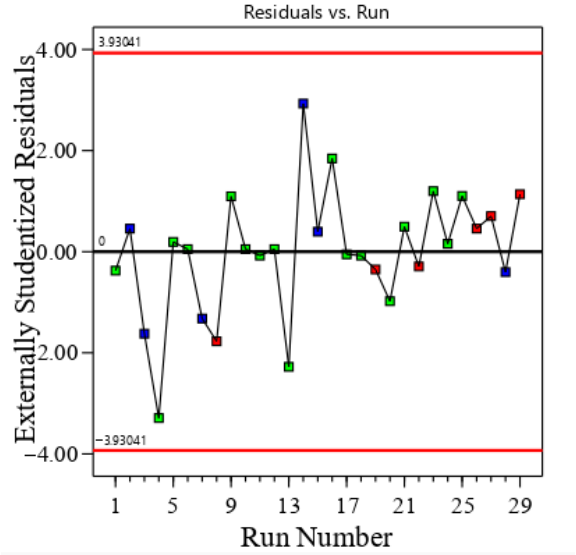
Figure 7 presents the relationship between residuals and experimental run order. It can be observed that the externally studentized residuals of all response variables are randomly distributed around the zero line and do not exhibit any continuous increasing, decreasing, or periodic trend with the experimental sequence. All residual values fall within the range of ±3, and no abnormal runs are identified. These results indicate that the experimental errors exhibit good independence, and the regression model is not affected by systematic time effects or experimental drift.




(**a**) 28-day flexural strength




(**b**) 28-day compressive strength

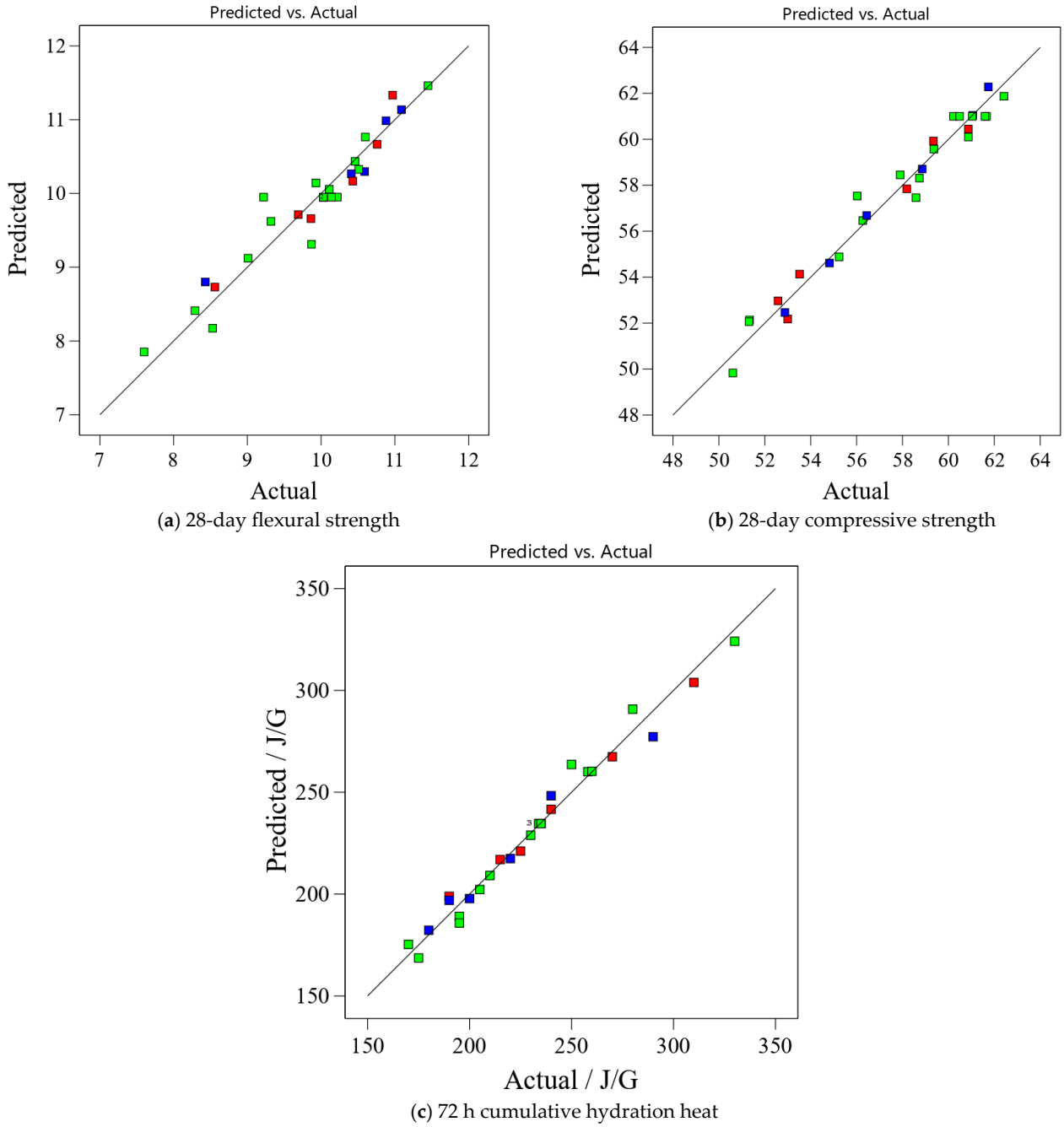



(**c**) 72 h cumulative hydration heat

**Figure 7.** Residual vs. run order plots for the 28-day flexural strength, 28-day compressive strength, and 72 h cumulative hydration heat of CWCM mortar specimens. (Blue, green, and red of the models for 28-day flexural strength ($Y_1$), 28-day compressive strength ($Y_2$), and 72 h cumulative hydration heat ($Y_3$), respectively).

### 3.4.4. Analysis of Predicted vs. Actual Values

Figure 8 compares the predicted values obtained from the response surface regression models with the corresponding experimental results for the 28-day flexural strength, 28-day compressive strength, and hydration heat of construction-spoil-based mortar specimens. As can be seen, the experimental data points are clustered around the line y = x, and most points lie close to this line, indicating a good agreement between predictions and measurements. This demonstrates that the proposed response surface models exhibit high consistency and satisfactory fitting performance, thereby supporting the reliability of the experimental results. Overall, the response surface regression models can be used to analyze and optimize the mechanical properties and hydration-heat characteristics of CWCM, enabling a synergistic optimization of multiple influencing factors.




(**a**) 28-day flexural strength

(**b**) 28-day compressive strength

(**c**) 72 h cumulative hydration heat

**Figure 8.** Comparison between predicted and experimental values for the 28-day flexural/compressive strength and 72 h cumulative hydration heat of construction-spoil-based mortar specimens. (Blue, green, and red of the models for 28-day flexural strength ($Y_1$), 28-day compressive strength ($Y_2$), and 72 h cumulative hydration heat ($Y_3$), respectively).

### *3.5. Response Surface Analysis*

According to the ANOVA results in Tables 4 and 5, the significance ($p$-value) ranking of interaction terms affecting the flexural strength of CWCM mortar is BC < CD < AD < other interactions, suggesting that the BC interaction is the most significant and exerts a comparatively larger influence on flexural strength. For compressive strength, the significance ranking of interaction terms is AB < CD < BD < other interactions. Specifically, the interaction terms AB ($p < 0.0010$), CD ($p < 0.0010$), BD ($p = 0.0012$), and BC ($p = 0.0225$) exhibit $p$-values below 0.05, indicating statistically significant interaction effects and a pronounced influence on compressive strength. In contrast, AC ($p = 0.7386$) and

AD ($p$ = 0.7685) are not significant ($p$ > 0.05), implying that these interactions contribute little to compressive strength. Accordingly, the following section focuses on the interaction terms with higher significance to elucidate how factor interactions govern the flexural and compressive strength of CWCM mortar specimens.

#### 3.5.1. Flexural Strength

Figure 9 indicates that the interaction between construction spoil content (B) and curing temperature (C) exerts a significant effect on the 28-day flexural strength ($p$ = 0.0225). The response surface analysis shows that under standard curing conditions (20 ± 1 °C), the 28-day flexural strength reaches a maximum of 11.5 MPa at a spoil content of 15%. This value not only satisfies the requirement specified in GB/T 200-2017 [25] for P.O 42.5 cement (≥6.5 MPa), but also represents a 17.3% increase compared with the reference cement mortar (9.8 MPa). When the spoil dosage exceeds 20%, the flexural strength decreases noticeably, dropping to 9.2 MPa at 30% replacement. This decline is mainly attributed to the increased proportion of unreacted inert constituents at higher replacement levels. Notably, the effect of curing temperature on flexural strength is non-linear; when the curing temperature increases to 60 °C, the flexural strength decreases significantly to 8.7 MPa (a reduction of 18.3%).

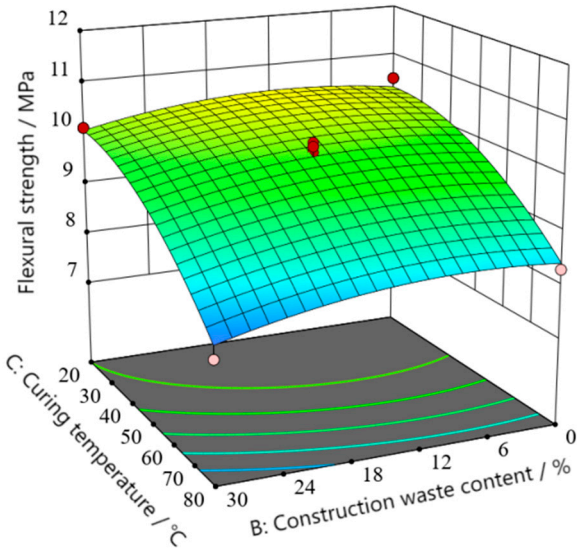



**Figure 9.** Response surface plots for the 28-day flexural strength.

#### 3.5.2. Compressive Strength

Figure 10 shows that the interaction between the water-to-binder ratio (A) and spoil content (B) has an extremely significant influence on compressive strength ($p$ < 0.001). The experimental results demonstrate that when the water-to-binder ratio is 0.275 and the spoil content is 15%, the 28-day compressive strength reaches 62.4 MPa. This value exceeds the strength requirement for P.O 42.5 cement (≥42.5 MPa) and approaches the strength level of P.O 52.5 cement. Sensitivity analysis further indicates that increasing the water-to-binder ratio by 0.05 leads to a 13.2% reduction in compressive strength, and this adverse effect becomes more pronounced under elevated curing temperatures. In addition, the strength reduction accelerates when the spoil content exceeds 20%. Based on the optimization results, the recommended ranges are a water-to-binder ratio of 0.26–0.29, a spoil content of 12–18%, and a curing temperature of 20–40 °C, under which the 28-day compressive strength can be maintained above 55 MPa.

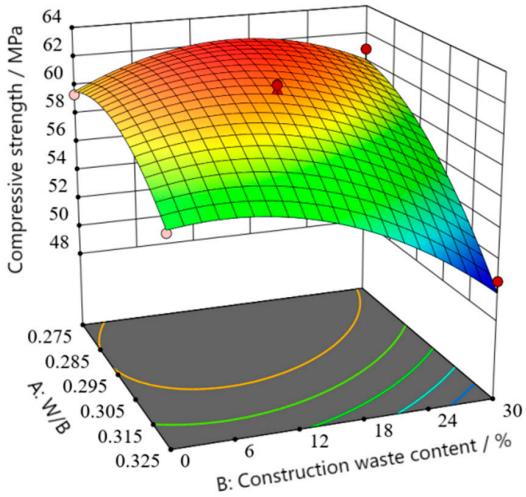



**Figure 10.** Response surface plots for the 28-day compressive strength.

### 3.5.3. Hydration Heat

According to the ANOVA results in Tables 4 and 5, the significance ranking (*p*-values) of interaction terms affecting the hydration heat of CWCM mortar is AC < BC < AB < other interactions. Specifically, AC ($p < 0.0016$), BC ($p = 0.0063$), and AB ($p = 0.0352$) are significant ($p < 0.05$), indicating that these interactions have pronounced effects on hydration heat. In contrast, AD ($p = 0.0835$) and BD ($p = 0.0692$) are not significant ($p > 0.05$), suggesting limited interaction effects on hydration heat.

Figure 11 further shows that the combined effect of the water-to-binder ratio (A) and curing temperature (C) on hydration heat is extremely significant ($p < 0.001$). Under the optimized conditions (water-to-binder ratio of 0.275 and spoil content of 15%), the 72 h cumulative hydration heat is 225 J/g, representing a 15.1% reduction relative to the reference P.O 42.5 cement paste (265 J/g) and meeting the hydration-heat criterion for low-heat cement specified in GB/T 200-2017 (≤230 J/g). In addition, at a spoil content of 15%, the occurrence time of the main exothermic peak associated with C3S hydration is delayed from 24 h to 32 h, while the peak heat flow decreases from 6.8 mW/g to 4.8 mW/g (a reduction of 29.3%). The curing temperature exerts a particularly strong influence on hydration heat; when the temperature increases to 80 °C, the 72 h cumulative hydration heat rises sharply to 310 J/g, implying a substantially elevated risk of thermally induced cracking due to increased temperature gradients.

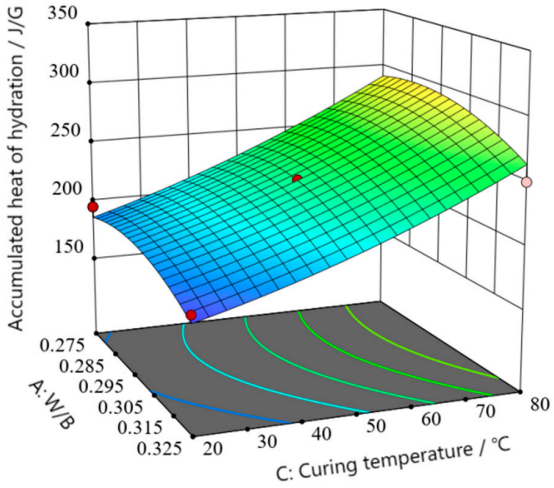



**Figure 11.** Response surface plots for the 72 h cumulative hydration heat.

To clarify the engineering significance of reducing cumulative hydration heat for mitigating early-age cracking in mass concrete, a simplified temperature rise–thermal stress model was introduced for discussion. The adiabatic temperature rise in mass concrete can be approximately expressed as:

$$\Delta T_{ad} = Q \times B/\rho \times c$$

where Q is the cumulative hydration heat per unit mass of binder (J/g), B is the binder content (kg/m$^3$), and ρ and c represent the density and specific heat capacity of concrete, respectively. In this study, the 72 h cumulative hydration heat decreased from 265 J/g to 225 J/g (a reduction of approximately 15.1%). Under the condition that B, ρ, and c remain constant, the theoretical adiabatic temperature rise ($\Delta T_a d$) would also decrease by approximately 15.1%, thereby reducing the temperature difference between the interior and surface of the structure.

Furthermore, the early-age thermal stress can be approximately expressed as:

$$\sigma_T \approx E(t)\alpha\Delta T$$

where E(t) is the age-dependent elastic modulus, $\alpha$ is the coefficient of thermal expansion, and ΔT represents the temperature difference. Therefore, reducing the cumulative hydration heat effectively lowers the temperature-induced tensile stress, thereby improving the cracking resistance safety margin. These results indicate that CWCM has potential advantages for temperature control and crack mitigation in mass concrete applications.

### *3.6. Experimental Validation*

Validation tests were conducted using the optimal mixture obtained from the response surface optimization (water-to-binder ratio = 0.275, construction spoil replacement = 15%, curing temperature = 28.1 °C, and ball-milling time = 5 min). The results show that the 28-day compressive strength and flexural strength reached 61.03 MPa and 11.17 MPa, respectively, meeting the strength-class requirements of P.O 52.5 and P.O 42.5 cement. Meanwhile, the 72 h cumulative hydration heat was 225 J/g, representing a 15.1% reduction compared with ordinary P.O 42.5 cement (265 J/g) and fully satisfying the criterion for low-heat cement in GB/T 200-2017 (≤230 J/g). The relative errors between the measured and predicted values for all responses were below 5%, confirming the reliability of the proposed models. These findings indicate that the developed binder can effectively serve as an alternative to conventional low-heat cement for mass-concrete applications.

### *3.7. Reliability Analysis*

To verify the reliability of the model predictions, experimental validation was conducted for the optimized mixture. The results show that the relative errors between predicted and experimental values are all below 2%, indicating high prediction accuracy of the model. In addition, the coefficient of determination $R^2$ exceeds 0.95, and the RMSE values are small, demonstrating a good fitting performance of the model. The 95% confidence intervals calculated from repeated experimental data show that all measured values fall within the predicted ranges, confirming the statistical reliability and stability of the response surface model.

### *3.8. Microstructural Analysis*

#### 3.8.1. XRD Analysis

Figure 12 illustrates the influence of construction spoil content on the hydration products of CWCM at 28 d. As shown, diffraction features corresponding to C–S–H, ettringite (AFt), $CaCO_3$, C–A–S–H, and $Ca(OH)_2$ appear at approximately 2θ = 11°, 18°,

28°, 32°, and 34°, indicating that the hydration products of construction-spoil-based binders are dominated by C–S–H, AFt, $CaCO_3$, C–A–S–H, and $Ca(OH)_2$. In the control mixture without construction spoil (0%), the main hydrates are C–S–H, AFt, $CaCO_3$, and $Ca(OH)_2$, and the diffraction characteristics are similar to those of conventional cement systems because hydration is mainly governed by the intrinsic hydration of the cementitious phase. When the spoil content is 15%, the characteristic peaks of AFt and $Ca(OH)_2$ become sharper and more intense, and the broadened diffuse hump associated with C–S–H and C–A–S–H gels is more pronounced, suggesting that the reactive $SiO_2$ and $Al_2O_3$ in the spoil actively participate in pozzolanic reactions. Specifically, reactive Si and Al from the spoil react with $Ca(OH)_2$ generated during hydration, which not only consumes part of $Ca(OH)_2$ but also promotes the formation of C–S–H and C–A–S–H gels [19]. In contrast, the peaks associated with inert minerals such as quartz and dolomite remain relatively weak, indicating that these phases are largely non-reactive. When the spoil content increases to 30%, the peaks of AFt, $Ca(OH)_2$, and $CaCO_3$ become sharper and further intensified, implying an increased amount of crystalline hydration products; however, an excessive accumulation of these crystalline phases may lead to a deterioration in the mechanical performance of CWCM.

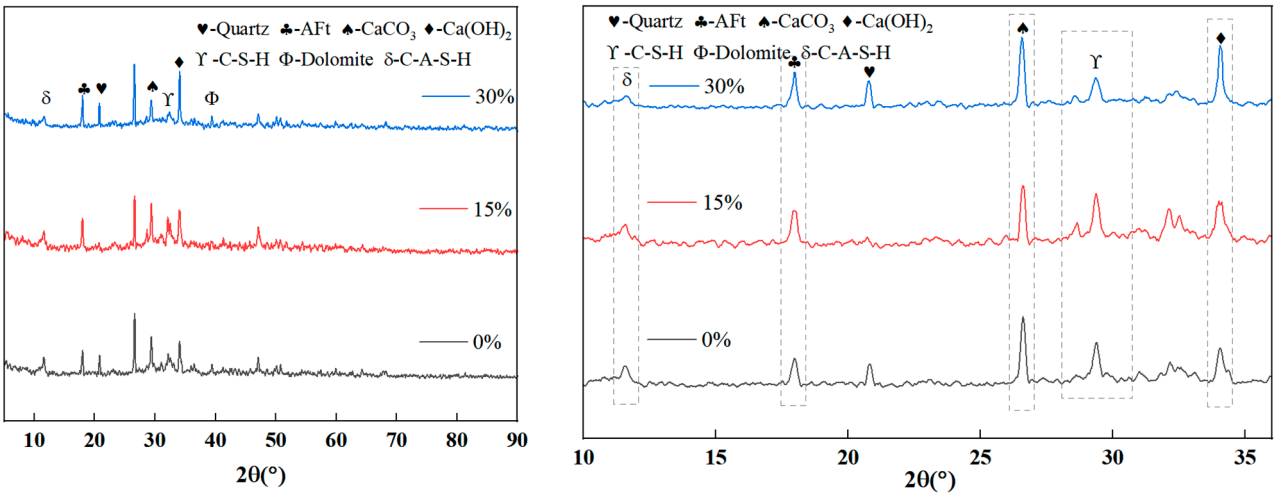
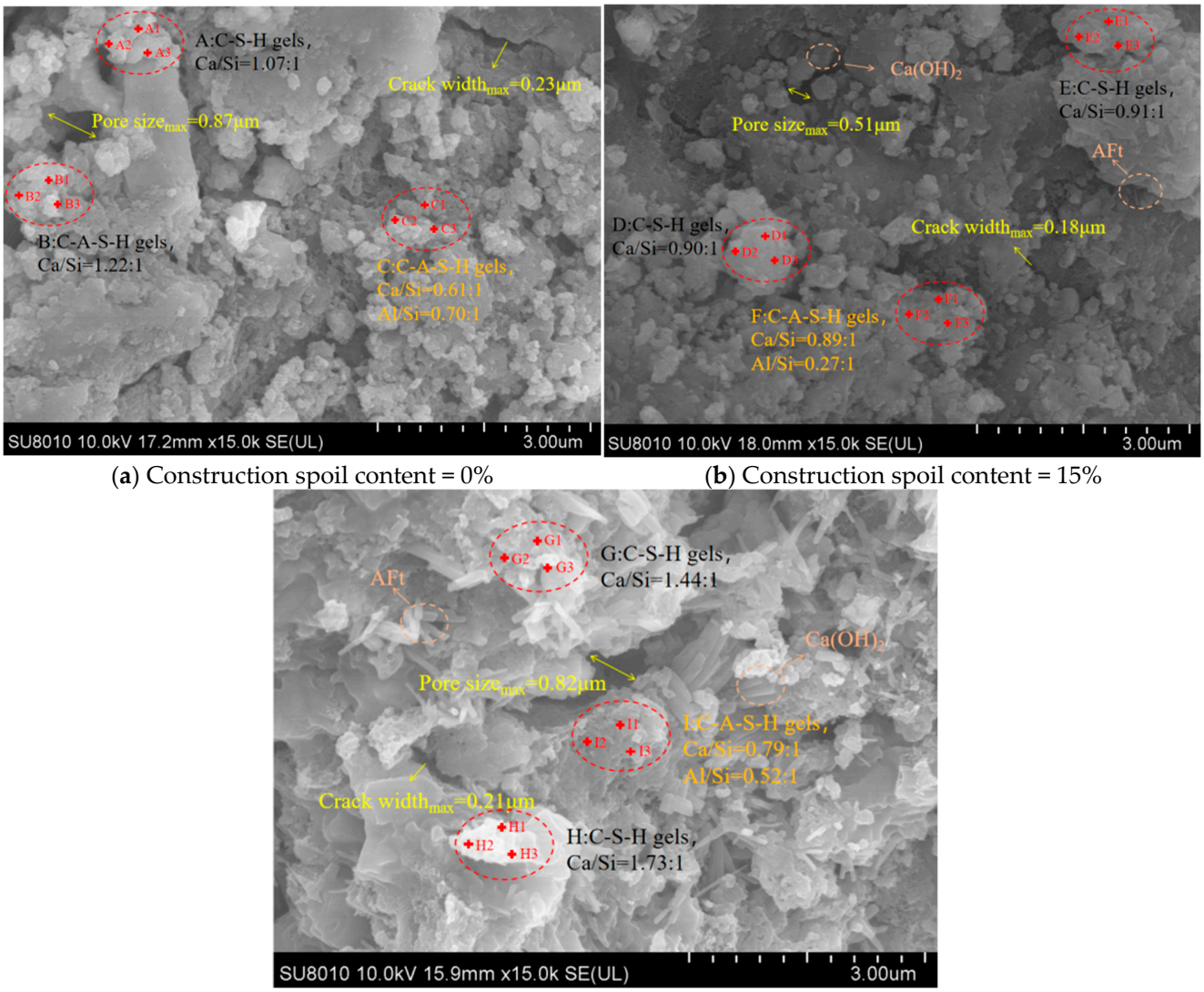



**Figure 12.** XRD patterns of CWCM at different construction spoil contents.

### 3.8.2. SEM Analysis

Figure 13 presents the 28-day micro-morphologies of hydration products of CWCM specimens incorporating different construction spoil contents (0%, 15%, and 30%). At 0% spoil, the microstructure is relatively loose, with a higher density of microcracks; the maximum crack width is 0.23 μm, the maximum pore size is 0.87 μm, and the hydrates are dominated by amorphous, agglomerated gel phases. According to the EDS results (Table 7), the reaction products in regions A and B mainly consist of Ca, Si, and O, with Ca/Si ratios of 1.07 and 1.22, respectively, which fall within the typical range reported for C–S–H gel (Ca/Si ≈ 0.5–1.8) [20]; therefore, the hydrates in regions A and B can be identified as C–S–H. In region C, the major elements are Ca, Si, Al, and O, with Ca/Si = 0.61 and Al/Si = 0.70, consistent with the characteristic compositional ranges of C–A–S–H gel (Ca/Si ≈ 0.6–1.4 and Al/Si ≈ 0.1–1.1). Combined with the XRD evidence for the presence of C–A–S–H in CWCM, the hydrates in this region are attributed to C–A–S–H gel. Moreover, Figure 13c shows abundant plate-like and prismatic crystalline phases, indicating the formation of ettringite (AFt) and $Ca(OH)_2$.




(**a**) Construction spoil content = 0% (**b**) Construction spoil content = 15%

(**c**) Construction spoil content = 30%

**Figure 13.** SEM micrographs of hydration products of the construction-spoil-based binder at different construction spoil contents.

**Table 7.** Statistical comparison between model predictions and experimental results.

| Parameter | Predicted Value | Experimental Value | Relative Error (%) | Standard Deviation | 95% CI |
|---|---|---|---|---|---|
| Compressive strength (MPa) | 60.85 | 61.03 | 0.29% | ±0.84 | 59.8–62.2 |
| Flexural strength (MPa) | 8.12 | 8.05 | 0.87% | ±0.21 | 7.9–8.2 |
| Hydration heat (J/g) | 228 | 225 | 1.33% | ±3.5 | 219–231 |

Comparing Figure 13a,b, increasing the spoil content from 0% to 15% reduces the maximum crack width from 0.23 μm to 0.18 μm and decreases the maximum pore size to 0.51 μm, implying a reduction in matrix porosity. As indicated by Table 8, the Ca/Si ratio of C–S–H decreases from ~1.2 to ~0.9, suggesting the formation of more low-Ca/Si C–S–H, which is generally associated with a denser microstructure. Such C–S–H can interconnect to form a continuous three-dimensional network that fills internal voids and thus refines the pore structure. Meanwhile, the Al/Si ratio of C–A–S–H decreases from 0.70 to 0.27, and a lower Al/Si ratio tends to favor a more stable C–A–S–H structure that can intergrow more effectively with C–S–H, further enhancing microstructural compactness. When the

spoil content is further increased to 30%, the Ca/Si ratio of C–S–H rises to 1.44 and 1.73, accompanied by the pronounced formation of plate-like and prismatic AFt and $Ca(OH)_2$ crystals. The accumulation of these crystalline products may induce local volumetric changes and disrupt the previously compact matrix. Although abundant C–A–S–H gel is still observed, its Al/Si ratio increases to 0.52; excessive Al incorporation may interfere with gel packing and promote overgrowth of AFt, thereby aggravating the development of microcracks and pores. Consequently, the maximum crack width increases from 0.18 μm to 0.21 μm, and the maximum pore size increases to 0.82 μm, indicating a substantial rise in porosity. Overall, a spoil content of 15% yields a denser microstructure with reduced defects, which is expected to enhance macroscopic properties such as strength and impermeability, whereas a spoil content of 30% enlarges microstructural defects (cracks and pores), leading to deterioration in mechanical performance and durability.

**Table 8.** Atomic ratios of major elements in hydration products at different construction spoil contents determined by EDS.

| Samples | Area | Number | O | Na | Mg | Al | Si | K | Ca | Ca/Si | Al/Si |
|---|---|---|---|---|---|---|---|---|---|---|---|
| 0% | A | Average | 56.33 | 3.74 | 2.99 | 2.93 | 12.18 | 0.30 | 13.03 | 1.07:1 | - |
| | B | Average | 53.68 | 1.14 | 5.46 | 0.89 | 14.26 | 0.13 | 17.35 | 1.22:1 | - |
| | C | Average | 42.44 | 1.74 | 0.53 | 9.09 | 12.73 | 0.36 | 7.76 | 0.61:1 | 0.70:1 |
| 15% | D | Average | 58.53 | 7.12 | 2.83 | 3.28 | 7.23 | 0.67 | 6.50 | 0.90:1 | - |
| | E | Average | 60.45 | 6.12 | 1.5 | 2.62 | 7.04 | 0.38 | 6.39 | 0.91:1 | - |
| | F | Average | 60.73 | 4.32 | 0.39 | 3.06 | 11.29 | 0.33 | 10.02 | 0.89:1 | 0.27:1 |
| 30% | G | Average | 47.87 | 0.38 | 4.65 | 6.58 | 12.66 | 0.27 | 18.25 | 1.44:1 | - |
| | H | Average | 24.01 | 0.68 | 0.91 | 4.30 | 18.77 | 1.32 | 32.56 | 1.73:1 | - |
| | I | Average | 20.62 | 8.13 | 3.01 | 2.44 | 25.87 | 1.13 | 20.45 | 0.79:1 | 0.52:1 |

#### 3.8.3. TG/DTG Analysis

Figure 14 shows the thermogravimetric (TG/DTG) results illustrating the influence of construction spoil content on the reaction products of CWCM. The TG/DTG curves can be divided into five main temperature intervals: Stage I (50–110 °C) corresponds to the loss of free water; Stage II (110–430 °C) is attributed to the release of bound water from hydration products such as C–S–H and C–A–S–H; Stage III (430–550 °C) represents the decomposition of portlandite ($Ca(OH)_2$), as evidenced by the characteristic DTG peak at approximately 450 °C; Stage IV (550–790 °C) is associated with secondary dehydration of C–S–H and C–A–S–H, with mass losses of 4.14% (0% spoil), 3.92% (15% spoil), and 4.41% (30% spoil); and Stage V (790–1000 °C) corresponds to the decomposition of $CaCO_3$ [20]. Table 9 presents the corresponding mass loss values for each stage under different spoil replacement ratios. When the spoil content increased from 0% to 15%, the mass loss in Stage I decreased from 1.14% to 0.82% (a 28.1% reduction), whereas the Stage II mass loss increased from 7.13% to 8.63% (a 21.4% increase), indicating an increased amount of gel-type hydrates (C–S–H/C–A–S–H). Meanwhile, the Stage III mass loss decreased from 2.77% to 2.35% (15.16% reduction), suggesting that reactive components in the spoil consumed part of $Ca(OH)_2$ via pozzolanic reactions, while a sufficient amount of $Ca(OH)_2$ remained to sustain alkalinity and support continued hydration. The Stage IV mass loss slightly decreased from 4.14% to 3.92%, implying a change in gel stability at elevated temperatures. Consistent with the SEM observations, increasing spoil content from 0% to 15% reduced the maximum crack width from 0.23 μm to 0.18 μm and decreased the maximum pore size to 0.51 μm, which can be attributed to the increased formation of C–S–H and C–A–S–H gels that fill cracks and pores and thus densify the matrix. In Stage V, the $CaCO_3$ decomposition-related mass loss increased from 0.42% to 0.52% (23.8% increase), indicating a higher $CaCO_3$ content

at 15% spoil, likely due to carbonation of C–S–H/C–A–S–H gels and $Ca(OH)_2$ that forms $CaCO_3$; therefore, increasing spoil content promotes the Stage V mass loss.

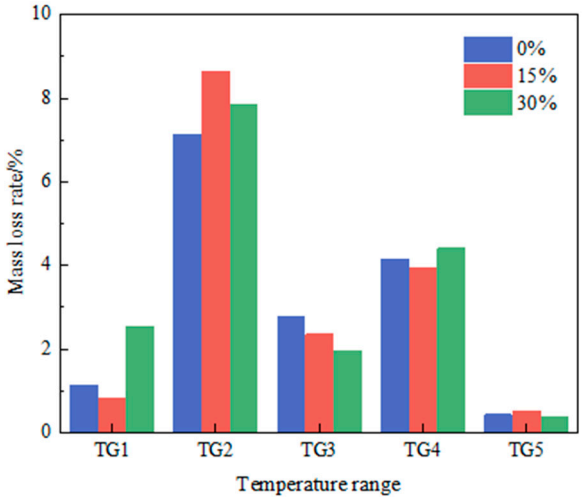



**Figure 14.** Mass loss of CWCM specimens in different temperature ranges under different spoil replacement ratios (%).

**Table 9.** Mass loss of CWCM specimens in different temperature ranges under different spoil replacement ratios (%).

| Temperature Range | Corresponding Stage | 0% Replacement | 15% Replacement | 30% Replacement |
|---|---|---|---|---|
| TG1 (50–110 °C) | Evaporation of free water | 1.14 | 0.82 | 2.53 |
| TG2 (110–430 °C) | Dehydration of C-S-H/C-A-S-H bound water | 7.13 | 8.63 | 7.85 |
| TG3 (430–550 °C) | Decomposition of $Ca(OH)_2$ | 2.77 | 2.35 | 1.96 |
| TG4 (550–790 °C) | Secondary dehydration of C-S-H/C-A-S-H | 4.14 | 3.92 | 4.41 |
| TG5 (790–1000 °C) | Decomposition of $CaCO_3$ | 0.42 | 0.52 | 0.38 |
| Total mass loss | Sum | 15.60 | 16.24 | 17.13 |

Figure 15 presents the TG/DTG analysis results of CWCM hydration products under different spoil replacement ratios. According to the thermal decomposition characteristics of cement-based materials, the TG/DTG curves can be divided into five stages:

- 50–110 °C corresponds to the evaporation of free water;
- 110–430 °C corresponds to the dehydration of bound water associated with hydration products such as C-S-H and C-A-S-H;
- 430–550 °C corresponds to the decomposition of calcium hydroxide ($Ca(OH)_2$), represented by the characteristic DTG peak at approximately 450 °C;
- 550–790 °C corresponds to the secondary dehydration of the gel structure;
- 790–1000 °C corresponds to the decomposition of $CaCO_3$ [21].

When the spoil replacement ratio increases from 0% to 15%, the mass loss in the first stage (free water evaporation) decreases from 1.14% to 0.82% (a reduction of 28.1%), indicating a reduction in free water storage space and a more compact pore structure. In the second stage (110–430 °C), the bound water mass loss increases from 7.13% to 8.63% (an increase of 21.4%), suggesting that the amount of structural bound water associated with C-S-H and C-A-S-H gels increases, reflecting enhanced formation of hydration gels. In the third stage (430–550 °C), the $Ca(OH)_2$ decomposition mass loss decreases from 2.77% to 2.35%. Based on the decomposition reaction $Ca(OH)_2 \rightarrow CaO + H_2O$ and the theoretical conversion equation CH (%) = 4.11 × ΔW, the calculated CH content decreases

from approximately 11.39% to 9.65%, indicating that the active $SiO_2$ and $Al_2O_3$ in the spoil participate in pozzolanic reactions and consume part of the $Ca(OH)_2$, while the system still maintains sufficient alkalinity to sustain hydration reactions. In the fourth stage (550–790 °C), the secondary dehydration mass loss slightly decreases from 4.14% to 3.92%, suggesting that moderate spoil addition does not significantly weaken the thermal stability of the gel structure at high temperatures. In the fifth stage (790–1000 °C), the $CaCO_3$ decomposition mass loss increases from 0.42% to 0.52% (an increase of 23.8%), which may be related to partial carbonation of CH and hydration products in the system.

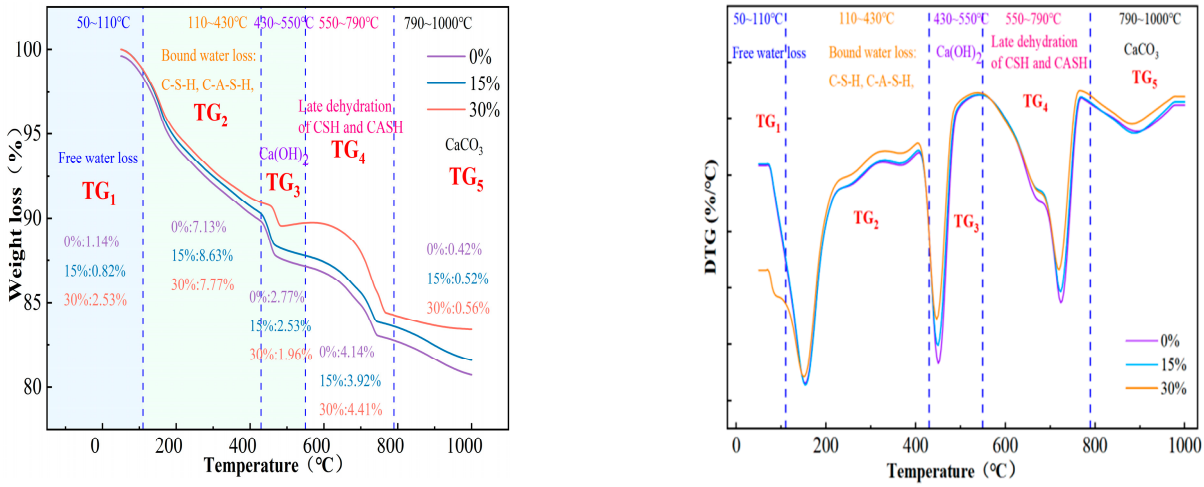



**Figure 15.** Effect of construction spoil content on the thermal mass loss of hydration products in CWCM.

When the spoil replacement ratio further increases to 30%, the free water mass loss in the first stage rises to 2.53%, significantly higher than that of the 15% group, indicating that excessive spoil addition may result in a looser pore structure and increased free water storage space. Meanwhile, the $Ca(OH)_2$ decomposition mass loss further decreases to 1.96%, corresponding to a CH content of approximately 8.05%, suggesting that excessive reactive components continue to consume CH, potentially weakening the alkaline environment and affecting later hydration reactions. The mass loss in the 550–790 °C range increases to 4.41%, indicating changes in the thermal stability of amorphous components under high replacement conditions.

Combined with SEM microstructural observations, the crack width and pore size at the 15% replacement level decrease to 0.18 μm and 0.51 μm, respectively, indicating the densest microstructure. In contrast, when the replacement ratio reaches 30%, the crack width increases to 0.21 μm and the pore size expands to 0.82 μm, suggesting significant deterioration of the pore structure. Overall, the combined TG/DTG quantitative analysis and microstructural observations indicate that at 15% spoil replacement, the bound water content increases, the CH content decreases moderately, and the pore structure becomes refined, demonstrating that the pozzolanic reaction is most effective under this condition, thereby promoting structural densification and performance enhancement. In contrast, excessively low or high replacement ratios reduce reaction efficiency or structural stability, which is unfavorable for the overall performance development of the material.

When the spoil content was further increased to 30%, the Stage I mass loss increased sharply from 0.82% to 2.53% (208.5% increase), indicating that excessive spoil addition promotes the development of pores and microcracks, enlarging the storage space for free water and thereby increasing the free-water content. The Stage III mass loss further decreased to 1.96%, implying continued consumption of $Ca(OH)_2$ and a potential

reduction in system alkalinity. The Stage IV mass loss increased to 4.41%, which may be related to additional dehydration of amorphous phases introduced by excessive spoil at high temperature. SEM observations consistently show that increasing the spoil content from 15% to 30% increased the maximum crack width from 0.18 μm to 0.21 μm and enlarged the maximum pore size to 0.82 μm. Overall, a spoil content of 15% improves the compactness of the CWCM microstructure and thus enhances mechanical performance, whereas overly low or overly high spoil contents increase porosity and lead to a decline in mechanical properties.

### *3.9. Correlation Analysis Between Micro and Macro Properties*

To further reveal the relationship between microstructural parameters and macroscopic performance, Table 10 summarizes the Ca/Si and Al/Si atomic ratios under different spoil replacement levels together with the corresponding compressive strength and hydration heat data.

**Table 10.** Comparison of Ca/Si and Al/Si ratios with mechanical properties and hydration heat.

| Scheme 28. | Ca/Si | Al/Si | 28-Day Compressive Strength (MPa) | 72 h Hydration Heat (J/g) |
|---|---|---|---|---|
| 0 | 1.85 | 0.12 | 53.2 | 265 |
| 10 | 1.45 | 0.18 | 58.6 | 238 |
| 15 | 0.90 | 0.23 | 61.03 | 225 |
| 30 | 1.60 | 0.15 | 48.7 | 210 |

The results indicate that as the Ca/Si ratio decreases from 1.85 to 0.90, the 28-day compressive strength increases from 53.2 MPa to 61.03 MPa, while the 72 h cumulative hydration heat decreases by approximately 15%. A lower Ca/Si ratio promotes the formation of a denser and more polymerized C-(A)-S-H gel structure, which enhances the load-bearing capacity of the matrix.

Meanwhile, the increase in the Al/Si ratio suggests that more Al atoms are incorporated into the gel framework, thereby improving the stability of the gel network. This trend is consistent with the reduction in hydration heat, indicating that the pozzolanic reaction promotes $Ca(OH)_2$ consumption and optimizes gel composition, which is a key mechanism for achieving the strength–low heat synergistic regulation.

Combined with XRD, SEM, and TG results, it can be further confirmed that at a spoil replacement level of 15%, the $Ca(OH)_2$ content decreases significantly, the bound water content increases, and the SEM images show a more uniform gel distribution with significantly reduced porosity. The synergistic effect of gel densification and pore structure refinement enhances the structural continuity of the material, thereby promoting strength development.

Therefore, the strengthening mechanism can be summarized as the following structural evolution pathway:

enhanced pozzolanic reaction → optimized gel composition → structural densification → improved load-bearing capacity.

### *3.10. Comparative Analysis and Scientific Discussion*

Compared with previous studies, the CWCM system developed in this work achieved a 28-day compressive strength of 61.03 MPa at a spoil replacement ratio of 15%, which is significantly higher than the 20–45 MPa range reported in many studies. A detailed comparison with other construction waste-based and supplementary cementitious material systems is presented in Table 11. Meanwhile, the 72 h cumulative hydration heat was

225 J/g, representing a 15.1% reduction compared with ordinary cement and satisfying the requirements for low-heat cement. These results indicate that the proposed system successfully achieves a balance between strength development and heat release control.

**Table 11.** Performance comparison of cementitious materials based on construction waste.

| Reference | Material Type | Replacement (%) | 28-day Compressive Strength (MPa) | Hydration Heat Reduction (%) |
|---|---|---|---|---|
| Wang et al. [9] | Spoil–cement | ≤20 | 20–30 | 10–15 |
| Chen et al. [17] | Calcined spoil system | 15–25 | 35–45 | 10–20 |
| He et al. [19] | Fly ash | 20 | 55–65 | 10–25 |
| Wang et al. [20] | Slag | 30 | 60–70 | 15–30 |
| This study | CWCM | 15 | 61.03 | 15 |

Microstructural analysis further reveals that, at a replacement ratio of 15%, the active $SiO_2$ and $Al_2O_3$ components in construction spoil effectively participate in the pozzolanic reaction, promoting the formation of low Ca/Si ratio C-(A)-S-H gel while consuming $Ca(OH)_2$. This process reduces early hydration heat release. TG/DTG results show that the bound water content increased by 21.4%, while SEM observations confirm a significant refinement of pore structure and a denser gel network. These microstructural changes represent the key mechanism underlying the synergistic regulation of strength and low hydration heat.

From an engineering perspective, traditional fly ash and slag systems can reduce hydration heat peaks by 10–30%, but their availability is strongly dependent on regional energy and steel production industries. In contrast, construction spoil, generated as a large-volume solid waste from urban infrastructure construction, is widely available and abundant. Under the optimized conditions identified in this study, its performance is comparable to that of some fly ash systems while offering superior advantages in waste recycling and resource utilization. Therefore, CWCM provides a promising new pathway for the sustainable development of low-heat cementitious materials in urban engineering applications.

## 4. Conclusions

In this study, CWCM was developed using construction spoil as the primary raw material. The mixture proportions were optimized via response surface methodology, and a combination of XRD, SEM, and TG/DTG analyses was employed to systematically investigate the mechanical performance, hydration-heat behavior, and hydration mechanisms of CWCM. The findings provide both theoretical insights and practical guidance for the high-value valorization of construction spoil and for the development of low-heat binders for mass-concrete applications. The main conclusions are as follows:

(1) Response surface optimization identified the optimal preparation parameters for CWCM as a water-to-binder ratio of 0.275, construction spoil replacement of 15%, curing temperature of 28.1 °C, and ball-milling time of 5 min. Under these conditions, CWCM achieved a 28-day flexural strength of 11.17 MPa and a 28-day compressive strength of 61.03 MPa, while the 72 h cumulative hydration heat was 225 J/g. The relative deviations between the measured and predicted values were all below 5%. The mechanical performance satisfies the requirements for strength class 42.5 cement and above, and the hydration heat was reduced by 15.1% compared with the reference P.O 42.5 cement, meeting the low-heat cement criterion specified in GB/T 200-2017 (≤ 230 J/g).

(2) The primary hydration products of CWCM include C–S–H, C–A–S–H, $Ca(OH)_2$, and ettringite (AFt). At a construction spoil content of 15%, the reactive $SiO_2$ and $Al_2O_3$

effectively consume $Ca(OH)_2$ through pozzolanic reactions and promote the formation of dense gels with low Ca/Si (0.89–0.91) and low Al/Si (0.27). Consequently, the maximum crack width decreases to 0.18 μm, and the maximum pore size is reduced to 0.51 μm, indicating a pronounced improvement in microstructural compactness, which in turn enhances both mechanical performance and low-heat characteristics.

(3) Construction spoil content plays a decisive role in regulating the performance of CWCM. At low replacement levels (< 15%), the pozzolanic reaction is insufficient; $Ca(OH)_2$ and AFt dominate the hydration products, and the microstructure remains relatively porous. At high replacement levels (> 15%), the fraction of inert constituents increases, the Ca/Si ratio of C–S–H rises to 1.44–1.73, and excessive formation of AFt and $Ca(OH)_2$ crystals may induce volumetric expansion, resulting in the enlargement of cracks and pores and a clear deterioration in mechanical performance and durability. Overall, CWCM enables high-value utilization of construction spoil while delivering a favorable balance of mechanical properties and low heat evolution. It therefore represents a viable alternative to conventional 42.5-grade cement for mass-concrete engineering, offering tangible environmental benefits by reducing spoil stockpiling and providing an effective strategy to mitigate thermal cracking associated with hydration heat, with substantial economic, environmental, and engineering value.

Based on the results of this study, the CWCM system satisfies the strength requirements of 42.5-grade cement while exhibiting a 72 h cumulative hydration heat of 225 J/g, which is significantly lower than that of ordinary P.O 42.5 cement and meets the requirements of GB/T 200-2017 for low-heat cement. Therefore, this material is particularly suitable for mass concrete structures requiring strict temperature control, such as hydraulic foundations, bridge pile caps, raft foundations, large equipment foundations, and underground structures. The use of CWCM can effectively reduce the risk of thermal cracking while improving structural durability and service safety.

It should be noted that practical engineering applications require a relatively stable raw material composition of construction spoil. A replacement ratio of $\leq$15% is recommended to ensure stable mechanical properties and microstructural performance. When the replacement ratio exceeds the reasonable range, the increased proportion of inert components may lead to higher porosity and deterioration in mechanical performance. Therefore, appropriate material testing and quality control measures should be implemented during practical applications.

## 5. Prospects

This study developed a low-heat composite cementitious material system based on construction spoil, achieving synergistic optimization between strength development and hydration heat regulation while revealing the corresponding microstructural evolution mechanisms. However, the large-scale engineering application of construction-waste-based cementitious materials still faces several challenges.

Future research should focus on the following aspects:

(1) Systematic evaluation of long-term durability, including carbonation resistance, freeze–thaw resistance, and chloride ion penetration resistance;
(2) Large-scale mass concrete model experiments or field engineering validation to evaluate temperature control performance and crack risk reduction;
(3) Development of predictive models to assess the influence of raw material composition variability and establishment of classification and applicability evaluation systems;
(4) Establishment of quantitative relationships between pore structure evolution and hydration heat release kinetics using multi-scale experimental techniques and numerical simulation;

(5) Life-cycle assessment (LCA) and carbon emission analysis to evaluate the low-carbon potential and environmental benefits of construction-spoil-based cementitious materials.

Through these studies, the proposed material system can be further promoted from laboratory optimization to practical engineering applications, enabling the high-value utilization of construction waste while enhancing structural performance and sustainability.

**Author Contributions:** Conceptualization, X.G.; Validation, C.W. and Z.S.; Formal analysis, D.J.; Writing—original draft, Q.Z.; Writing—review & editing, X.G. and H.W.; Visualization, C.W. and Z.S.; Supervision, H.W. and Z.S.; Project administration, D.J.; Funding acquisition, Q.Z. All authors have read and agreed to the published version of the manuscript.

**Funding:** This research received no external funding.

**Data Availability Statement:** The original contributions presented in the study are included in the article, further inquiries can be directed to the corresponding author.

**Conflicts of Interest:** Authors Xiangsai Guo, Desheng Jin, Chao Wang and Zhiwei Song were employed by the company China Railway 16th Bureau Group Co., Ltd. The remaining authors declare that the research was conducted in the absence of any commercial or financial relationships that could be construed as a potential conflict of interest.

## References

1. He, J.; He, J.; Wang, Y.; Fan, Y.; Shi, H.; Cai, B.; Yan, G. Research on the peak carbon emission pathway of China's cement industry. *Res. Environ. Sci.* **2022**, *35*, 347–355.
2. Zhang, Y.; Zhang, H.; Li, H.; Li, B.; Xu, Z.; Liu, Z. Influence of temperature rise inhibitors on early-age cracking of concrete: Evidence from temperature stress testing machine (TSTM) and restrained ring tests. *Constr. Build. Mater.* **2025**, *500*, 144218. [CrossRef]
3. Mo, Y.Y.; Tang, W.; Zhan, B.J.; Kou, S.C.; Xing, F. Performance and carbon footprint evaluation of carbonated recycled powder cement-based materials. *J. Build. Mater.* **2023**, *26*, 1207–1213.
4. Cavalett, O.; Watanabe, M.D.B.; Voldsund, M.; Roussanaly, S.; Cherubini, F. Paving the way for sustainable decarbonization of the European cement industry. *Nat. Sustain.* **2024**, *7*, 568–580. [CrossRef]
5. Huang, Q.; Dou, Y.; Zhang, D.; Zhou, W. Preparation and parameter optimization of filling cementitious materials using low-quality slag and fly ash. *China Min. Mag.* **2023**, *32*, 127–133.
6. Jiang, D. Application of construction spoil as subgrade filling material. *Sichuan Build. Mater.* **2023**, *49*, 21–22.
7. Wang, F.J.; Zhao, L.; Liang, Y.; Ma, G.P.; Liu, H.H.; Yang, T.T. Study on mix proportion parameters of stabilized soil prepared from construction spoil. *Build. Technol.* **2021**, *52*, 801–804.
8. Liu, Y.M.; Tang, J.R.; Li, H.; Zhang, W.H. Preparation of ceramic materials using construction solid waste. In Proceedings of the Annual Conference of the Chinese Society for Environmental Sciences, Beijing, China, 26–27 May 2024.
9. Wang, H.L.; Li, C.; Rong, H.; Song, W.J.; Qi, Z.G.; Li, X.H.; Di, Z.K. Influence of construction spoil on the performance of C30 concrete. *Bull. Chin. Ceram. Soc.* **2016**, *35*, 3030–3035.
10. Pan, D. Study on the Influence of Ground Construction Spoil on Hydration and Properties of Cement-Based Materials. Master's Thesis, Southeast University, Nanjing, China, 2019.
11. Guo, S.H.; Zhan, S.Z.; Kang, T.B.; Ding, X.Q.; Wang, F.C. Experimental study on mechanical and road performance of stabilized construction spoil. *Bull. Chin. Ceram. Soc.* **2024**, *43*, 4261–4269.
12. Jiang, S. Performance of cement-stabilized graded crushed stone mixtures with different construction waste contents. *Subgrade Eng.* **2023**, *3*, 95–101. [CrossRef]
13. Yang, T.; Li, X.R.; Liu, S.L.; Zhao, H.; Yan, M.M. Experimental study and micro-mechanism analysis of mechanical properties of stabilized spoil materials. *Chin. J. Undergr. Space Eng.* **2024**, *20*, 848–856.
14. Wang, H.L.; Zhao, Y.B.; Rong, H.; Zhu, X.Q.; Zhang, L.; Zhang, Y.; Gao, G.B. Influence of preparation process on the properties of concrete containing engineering spoil. *Bull. Chin. Ceram. Soc.* **2018**, *37*, 2526–2530.
15. Cao, K. Hydration characteristics of Composite Cementitious Materials Composed of Waste Clay Brick Powder, Metakaolin and Cement. Master's Thesis, Anhui University of Science and Technology, Huainan, China, 2021.
16. Wang, J. Application of Metakaolin Mineral Admixture in Low-Heat Early-Strength Concrete. Master's Thesis, Southwest University of Science and Technology, Mianyang, China, 2021.

17. Chen, D.; Song, X.; He, Z. Effects of calcined spoil–dolomite on strength and expansion properties of cement mortar. *J. Yangtze River Sci. Res. Inst.* **2021**, *38*, 146–150.
18. *GB/T 17671-2021*; Method of Testing Cements—Determination of Strength (ISO Method). Standardization Administration of China: Beijing, China; Standards Press of China: Beijing, China, 2021.
19. He, J.; Wu, J.; Ren, H.; Sang, G.; Dong, Z.; Jin, R. Physical–mechanical properties and solidification mechanism of fluid-solidified muck prepared with whole solid waste and construction muck. *Constr. Build. Mater.* **2025**, *465*, 140221. [CrossRef]
20. Wang, A.G.; Zheng, Y.; Zhang, Z.H.; Liu, K.W.; Li, Y.; Shi, L.; Sun, D.S. Comparison of durability between alkali-activated materials and ordinary Portland cement and concrete. *Engineering* **2020**, *6*, 237–261. [CrossRef]
21. Dong, J.; Zhang, T.; Zhu, Y.; Zhang, L.; Jiang, Y.; Zhu, J. Synthesis of alkali-activated uncalcined Pisha sandstone cement composites. *Compos. Part B Eng.* **2021**, *225*, 109240. [CrossRef]
22. Zhang, C.; Wang, D.; Shi, X.; Li, T.; Sun, G.; Liang, R. Effect of superabsorbent polymer on shrinkage and hydration of high-performance cement-based composites. *Mater. Rep.* **2024**, *38*, 196–202.
23. Zhang, Y. Simulation analysis of hydration heat in mass concrete for special-shaped pile caps of cross-sea bridges. *Tianjin Constr. Sci. Technol.* **2026**, *36*, 5–10.
24. Tan, Y.Q.; Hong, L.; Zhu, L.L.; Zhao, D.; Li, H.C. Experimental study on mechanical properties and microstructure of fly ash-slag based geopolymer cementitious materials. *J. Hefei Univ. Technol.* **2026**, *49*, 268–277.
25. Ma, Z.C.; Yao, Y.; Wen, Z.J.; Gao, X. Introduction of revisions in GB/T 200—2017. *Cement* **2018**, *12*, 57–58. [CrossRef]

**Disclaimer/Publisher's Note:** The statements, opinions and data contained in all publications are solely those of the individual author(s) and contributor(s) and not of MDPI and/or the editor(s). MDPI and/or the editor(s) disclaim responsibility for any injury to people or property resulting from any ideas, methods, instructions or products referred to in the content.